# Can the 2D shallow water equations model flow intrusion into buildings during urban floods?

Benjamin Dewals[1], Vasileios Kitsikoudis[2], Miguel Angel Mejía-Morales[3], Pierre Archambeau[1], Emmanuel Mignot[4], Sébastien Proust[3], Sébastien Erpicum[1], Michel Pirotton[1], André Paquier[3]

[1] Hydraulics in Environmental and Civil Engineering, Urban and Environmental Engineering, University of Liege, 4000 Liege, Belgium

[2] Water Engineering and Management, Faculty of Engineering Technology, University of Twente, 7500 AE Enschede, The Netherlands

[3] UR RiverLy – INRAE, 5 rue de la Doua CS 20244, 69625 Villeurbanne, France

[4] University of Lyon, INSA Lyon, CNRS, LMFA, Ecole Centrale Lyon, Université Claude Bernard Lyon 1, UMR5509, F-69621 Villeurbanne, France

## Abstract

The multiple flow paths existing in urban environments lead to complex flow fields during urban flooding. Modelling these flow processes with three-dimensional numerical models may be scientifically sound; however, such numerical models are computationally demanding. To ascertain whether urban floods can be modelled with faster tools, this study investigated for the first time the capacity of the 2D shallow water equations (SWE) in modelling the flow patterns within and around urban blocks with openings, i.e., involving flow exchanges between the flows in the streets and within the urban blocks (e.g., through alleys leading to courtyards or through broken windows or doors). Laboratory experiments of idealized urban floods were simulated with two academic 2D SWE models, with their most notable difference being the parameterization of the eddy viscosity. Specifically, the first model had a zero-order turbulence closure while the second model had a second-order depth-averaged $k$-$\varepsilon$ turbulence closure. Thirteen urban layouts were considered with steady flow and five with unsteady flow. Both models simulated the flow depths accurately for the steady cases. The discharge distribution in the streets and the flow velocities were predicted with lower accuracy, particularly in layouts with large open spaces. The average deviation of the modelled discharge distribution at the outlets was 2.5% and 7.3% for the first and second model, respectively. For the unsteady cases, only the first model was tested. It predicted well the velocity pattern during the falling limb of a flood wave, while it did not reproduce all recirculation zones in the rising limb. The peak flow depths in the streets and the peak discharges at the outlets were predicted with an average deviation of 6.7% and 8.6%, respectively. Even though some aspects of the flow in an urban setup are 3D, the findings of this study support the modelling of such processes with 2D SWE models.

**Keywords**

Experimental hydraulics; Numerical modelling; Open channel flow; Shallow water equations; Turbulence; Urban flood

## 1. Introduction

Urban flood risk is a growing concern (Addison-Atkinson et al., 2022; Chen et al., 2015; Doocy et al., 2013) given the high urbanization rate (Birkmann et al., 2016; Chen et al., 2022; Gross, 2016) and the intense anticipated rainfall events due to climate change (Hettiarachchi et al., 2018; Pfahl et al., 2017; Sanderson et al., 2019). The flood risk mapping of an urban area remains a challenging task due to the variability in the direct and indirect flood impacts (Kreibich et al., 2014) and in the flood vulnerability (Chen et al., 2019; Huggel et al., 2013; Lv et al., 2022) associated with various socioeconomic contexts in different parts of a city, as well as due to intricate urban layouts that induce complex flow patterns influencing the flood hazard (Leandro et al., 2016; Li et al., 2021a; Lin et al., 2021).

Urban flood numerical modelling is a vital component of flood risk assessment (Rosenzweig et al., 2021) and management (Guo et al., 2021; Jongman, 2018), and supports design strategies for sustainable and resilient urban infrastructures (Qi et al., 2022; Zhou et al., 2018). Contrary to one-dimensional (1D) (Kitsikoudis et al., 2020) and 1D-2D (Bates, 2022) simplifications that can be made in river modelling aiming mostly at estimating inundation extents, numerical modelling of multidirectional flows in flooded urban areas should be at least 2D (Li et al., 2021a; Mignot et al., 2006), with a focus on the spatial distribution of not only flow depths but also flow velocities (Kreibich et al., 2009) and specific discharges (Costabile et al., 2020) to express the flood hazard degree in the street network. This is particularly true for large impervious surfaces upstream of and in urban areas that can lead to an excessive amount of runoff, which cannot be conveyed by the drainage systems. Such high flow discharges may threaten the stability of pedestrians (Arrighi et al., 2017; Bernardini et al., 2020; Postacchini et al., 2021; Xia et al., 2014) and can cause the entrainment of vehicles (Martinez-Gomariz et al., 2018; Smith et al., 2019; Xia et al., 2011). Hence, the accurate spatial quantification of hydraulic variables within an urban area is of utmost importance.

### ***1.1.*** *Role of laboratory experiments for model validation*

A large number of numerical modelling studies simulated urban flows in real-world cases (Guo et al., 2021; Luo et al., 2022), with some of them using LiDAR data with high-resolution digital elevation models of the urban topography (Almeida et al., 2018; Ozdemir et al., 2013; Yalcin, 2020). However, validation field data including both flow depths and velocities are usually lacking or insufficient (Costabile et al., 2020), which may lead to equifinality issues. Remote sensing techniques can provide inundation extents and water levels, although with certain limitations as tall buildings within the urban environment may obscure some measurements (Neal et al., 2009), but flow velocity measurements in urban floods are more challenging. Such measurements are dangerous and can be costly, and as a result, are limited (Brown and Chanson, 2013). Flow depths and surface velocities can alternatively be determined by monitoring parts of a flooded urban area with unmanned aerial vehicles (Perks et al., 2016) and by analyzing existing footage and crowdsourced data from flooded street networks (Mignot and Dewals, 2022; Re et al., 2022). However, there are uncertainties related to the boundary conditions in complex urban terrains with large spatial variability and to the interplay between surface flow and flow in underground drainage systems (Bazin et al., 2014; Chang et al., 2018; Kitsikoudis et al., 2021; Rubinato et al., 2022). Finally, the typically short duration of pluvial flooding and its local character do not allow for detailed measurements over long durations. Experimental measurements in laboratory facilities provide an alternative option for models' validation. In carefully designed experiments, the flow and boundary conditions can be accurately controlled (Mignot et al., 2019) and besides offering a better understanding of the governing physical processes, such studies can contribute to the validation of numerical models, which may subsequently be used for scenario analyses of field cases.

### ***1.2.*** *Performance of 2D shallow water models*

The 2D shallow water equations (SWE) can be used to simulate the flow in flooded streets, with typically large width-to-depth ratios. However, at street intersections the interacting flows coming from various branches generate complex patterns (Mignot et al., 2008) and 3D flow structures (El Kadi Abderrezzak et al., 2011; Ramamurthy et al., 2007). While 3D models can capture most features of diverging flows in bifurcations (Mignot et al., 2013; Neary et al., 1999; Ramamurthy et al., 2007) and converging flows in junctions (Huang et al., 2002; Luo et al., 2018; Schindfessel et al., 2015), it is important to examine whether these flow processes can be satisfactorily reproduced by 2D operational models that are much faster than 3D models and can be used for real-time modelling. The 2D SWE approach has been proven capable to replicate experimental measurements of flow depths and discharge partitioning in bifurcations (Bazin et al., 2017; El Kadi Abderrezzak and Paquier, 2009; Khan et al., 2000; Li et al., 2021b; Shettar and Murthy, 1996), in junctions (Li et al., 2021b), in crossroads (Mignot et al., 2008), as well as in larger and more complicated street networks such as that of Arrault et al. (2016) with 49 intersections and that of Li et al. (2021b) with four intersections. Li et al. (2021a) incorporated various urban layouts in their experimental setup and also modelled successfully the flow depths and discharge partition with a 2D SWE model.

Despite the successful applications of 2D SWE in modelling water surface profiles and discharge distributions, some open questions remain (Li et al., 2020) regarding the accuracy of 2D SWE in predicting flow velocities in intersections, the extents of recirculating flow areas occurring due to flow separation in some of the branches, and the role of the turbulence closure model (Rodi, 2017). Shettar and Murthy (1996) modelled depth-averaged flow velocities in a bifurcation with a $k$-$\varepsilon$ turbulence closure and their modelled velocities in the main channel and the length of the recirculation zone agreed well with the experimental measurements. However, their modelled velocities in the branch of the bifurcation were less accurate. Khan et al. (2000) also modelled the flow in a bifurcation but with a mixing length model and reported that the modelled depth-averaged velocities compared well with the measurements, while the dimensions of the recirculation zone were predicted by the model satisfactorily. Bazin et al. (2017) used a constant eddy viscosity model to simulate flows in a bifurcation with a branch with a 90 degree angle, with and without obstacles at the intersection, and the modelled depth-averaged flow velocities in the recirculation zone on the upstream side of the bifurcation branch deviated from the measurements. Bruwier et al. (2017) argued that a $k$-$\varepsilon$ turbulence closure model should be more suitable than a constant eddy viscosity model for modelling flow interactions in intersections, given that since a $k$-$\varepsilon$ model does not necessarily require calibration, its computational demand can be similar to a constant eddy viscosity model that requires calibration. Arrault et al. (2016) showed in a more complex setup that the turbulence closure model was not particularly influential in the estimation of discharge distribution in the various streets; however, a $k$-$\varepsilon$ turbulence closure model modified significantly the estimates of the recirculation lengths compared to a simulation without a turbulence model. No velocity measurements were available, however, to compare the modelled velocities. More recently, Li et al. (2021a) modelled depth-averaged velocities in an urban district with various urban forms with a $k$-$\varepsilon$ turbulence closure model and achieved good agreement with surface velocities in areas of flow contraction, however, the results were less accurate in large open areas. Supercritical (Bazin et al., 2017; Mignot et al., 2008) and transcritical (El Kadi Abderrezzak et al., 2011) flows in crossroads may pose additional challenges in 2D SWE models, since the occurrence and structure of hydraulic jumps can significantly affect the discharge partitioning and water surface profiles.

### ***1.3.*** *Flow intrusion into buildings: an extra challenge*

Numerical and experimental studies of urban flooding typically consider flow around non-porous residential blocks (Haltas et al., 2016; Van Emelen et al., 2012). However, in reality urban blocks may have corridors leading to backyards, while during intense flooding windows and doors (labeled as "openings" from now on) of buildings may break, leading to lateral flow exchanges between a street and the inside area of the buildings (Mignot et al., 2020) causing significant damages in their interiors (Dottori et al., 2016; Martinez-Gomariz et al., 2021). Mejia-Morales et al. (2021) conducted a systematic experimental analysis of the effect of the location and size of openings in an urban block located within an idealized urban district. They showed that the flow exchanges between the streets and the block interior can alter the flow depth and the flow velocity in the surrounding streets by 12% and 70%, respectively, when compared to a reference case with a non-porous block. Besides the recent study of Mejia-Morales et al. (2021), there is only a limited number of studies that investigated how the porosity of urban blocks affects the hydraulic characteristics of a flood. Mignot et al. (2020) measured the flow discharge entering a building through an open door, window, or gate in case of an urban flood, and they noticed that in some cases the intruding discharge can be approximated by formulas for side weirs. However, the authors also observed that this intruding discharge can be significantly affected by surrounding urban obstacles. Wüthrich et al. (2020) showed with a flume experiment how the hydrostatic force and the form drag exerted by a steady flow on a building are modified by the porosity and the orientation of the building, while Sturm et al. (2018) measured the flood impact forces on physical models of buildings with openings on a torrential fan. In other experiments, Liu et al. (2018) showed how the orientation of a house with respect to the incoming flow affects the forcing on the house door for a dam-break case and Zhou et al. (2016) found differences in the wakes of simplified porous and non-porous buildings. In a numerical study of a torrential flood, Gems et al. (2016) modelled how the different openings of a building affect the flow pattern within its interior, the associated hydrodynamic forcing, and the near-building flow pattern. The findings of these studies show that the openings in buildings affect the spatial distribution of flood hazard and thus the number and types of openings should be considered in flood modelling.

### *1.4. Objective of the study*

The flow exchanges between a street and the interior of a building, in combination with bifurcations and junctions at crossroads, lead to complex and potentially 3D flow patterns around urban blocks during urban floods. Since urban areas are typically densely populated, there is a need for fast computational tools that could be utilized for real-time modelling of not only the flow depths but also the flow velocities for the accurate estimation of the flood hazard. 3D numerical models can potentially capture the flow processes of urban floods; however, they are computationally demanding and slow for real-time modelling. In practice, the 2D SWE are used for operational flood hazard and risk modelling. While previous studies have already analysed the ability of the 2D SWE to simulate flow fields in various settings, such as bifurcations, junctions, 4-branch crossroads, and street networks, they all assumed that the street boundaries (i.e., building facades) were impervious. No existing study has focused on the performance of the 2D SWE to predict the flow intrusion into flooded buildings or building blocks, nor on the flow patterns in the streets and within the urban blocks in urban configurations with openings in the building facades.

The objective of this study is to examine, for the first time, whether the flow patterns within and around porous urban blocks (i.e., with openings) can be quickly and accurately predicted with numerical modelling based on 2D SWE and to determine what is the most effective modelling strategy for the accurate estimation of flow velocities and flow depths. To this end, the experiments of Mejia-Morales et al. (2021) and Mejia-Morales et al. (2022a) for flow around and within a porous urban block are replicated using two different academic numerical modelling tools to investigate the importance of eddy viscosity parameterization on the accuracy of the models. Complementary steady flow experiments with additional geometric configurations are also presented for the first time, based on the same experimental approach as Mejia-Morales et al. (2021). The paper is organized as follows: in Section 2, the experimental procedure is briefly described, and the numerical models are presented. The new experimental results and the results of the numerical modelling are presented and discussed in Section 3. Finally, conclusions are drawn in Section 4.

## 2. Experiments and numerical modelling

This section presents the experimental setup (Section 2.1), the various porous urban block configurations that were tested (Section 2.2), the numerical models that were used to simulate the experimental data (Section 2.3), and the prescribed boundary and initial conditions (Section 2.4). Both steady and unsteady flow conditions were simulated with the numerical models. For steady flow conditions, the experimental data are a combination of the data presented by Mejia-Morales et al. (2021) and new data collected from the same urban physical model in the same facility. For unsteady flow conditions, the experimental data of Mejia-Morales et al. (2022a) are used. Only a brief overview of the experimental setup and methods is provided here since they are described in detail in the aforementioned papers.

### ***2.1.*** *Experimental setup*

Mejia-Morales et al. (2021) and Mejia-Morales et al. (2022a) experimentally investigated urban floods at the city block scale using a physical model of a rectangular urban block surrounded by four streets, under steady (Figure 1a) and unsteady (Figure 1b) flow conditions. For the steady flow experiments, the length of the two streets in the *x*-direction (named “Right Street” and “Left Street”) was 5.4 m and the length of the two streets in the *y*-direction (named “Downstream Street” and “Upstream Street”) was 3.2 m. All four streets had the same rectangular cross section with a width $b$ = 0.15 m. The experimental setup for the unsteady flow experiments was the same, except for the initial part of the Left Street, which was closed upstream of the Upstream Street (Figure 1b). The physical model had a slope $S_{0,x} = 0.12\%$ in the *x* direction and $S_{0,y} = 0\%$ in the *y* direction, whereas the bed of the model was constructed with PVC and the sidewalls of the streets and the urban block were constructed with plastic. Various configurations of the urban block were tested (Section 2.2 and Figure 2); however, its total lengths in the *x* and *y* directions remained fixed at $L_x$ = 1.56 m and $L_y$ = 0.96 m, respectively. The thickness and the height of the walls of the porous block were 2 cm and 15 cm, respectively.

The model inlets were located at the upstream ends of the streets in the *x* direction. As such, the steady flow experiments had two inlets with fixed inlet discharges $Q_{\mathrm{in}_1}$ and $Q_{\mathrm{in}_2}$ for the Right Street and Left Street, respectively, while for the unsteady experiments discharge was fed only through the Right Street since the upstream reach of the Left Street was closed. The inlet discharges were measured using separate valve-flowmeter systems with an accuracy of 3%. Smooth inlet conditions were secured by placing a plastic honeycomb grid at the point entrance of the Right Street and of the Left Street. Each one of the four streets of the physical model had an outlet with a vertical tail weir that regulated the flow depth. For the steady flow cases, the weir height of Outlet 1 in the Right Street was 4 cm and of Outlet 2 in the Left Street was 3 cm, with respective outlet discharges $Q_{\mathrm{out}_1}$ and $Q_{\mathrm{out}_2}$. In the two streets in the *y* direction, the Outlet 3 in the Downstream Street and the Outlet 4 in the Upstream Street had the same 3 cm weir height, with outlet discharges $Q_{\mathrm{out}_3}$ and $Q_{\mathrm{out}_4}$, respectively. For the unsteady flow cases, the weir height was set to zero in all outlets to avoid the reflection of the floodwaves on the weir. The outflow discharges at the four outlets were monitored using electromagnetic flowmeters. Specifically, the water overflowing the weir in each outlet was collected in a separate tank and subsequently the flow exiting each tank was measured with an OPTIFLUX 2000 flowmeter, manufactured by KROHNE.

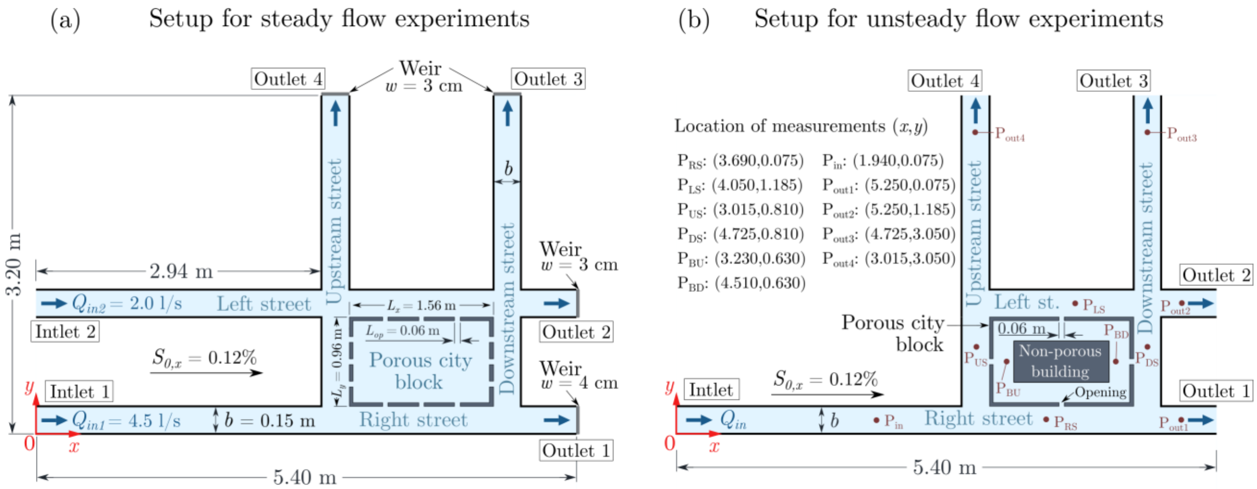


**Figure 1.** (a) Experimental setup for the steady flow experiments (adapted from Mejia-Morales et al. (2021)) and (b) experimental setup for the unsteady flow experiments (adapted from Mejia-Morales et al. (2022a)). In (b) the locations of measurements denote the points where flow depths were recorded for the whole duration of the hydrograph.

The flow depths in the physical model were measured using ultrasonic distance-measuring sensors (BAUMER UNDK 20I6914/S35A) with a 0.65 mm uncertainty. For the steady flow cases, a sensor was attached on a mechanical gantry system that allowed horizontal movement, with measurements being taken every 5 cm along the longitudinal direction of each street and at three locations across the street width with 6.5 cm spacing. Flow depth measurements within the porous urban block were conducted every 12 cm in both *x* and *y* directions. Each depth measurement was conducted with a sampling frequency of 50 Hz for a duration of 50 s (Mejia-Morales et al., 2021). For the unsteady flow cases, flow depths were measured at the eleven locations depicted in Figure 1b for the whole duration of each hydrograph. The reported flow depths are the results of ensemble averaging of 50 identical floodwaves that were fed sequentially into the model, with a steady base flow separating two sequential floodwaves. The number of required repeated floodwaves was selected by increasing the number until the ensemble average standard deviation of the flow depth became smaller than 1 mm. The floodwaves characteristics are detailed in Section 2.4.

For the steady flow cases, surface flow velocities were measured using large-scale particle image velocimetry (LSPIV) (Fujita et al., 1998). Floating wood shavings (1 - 4 mm) were used as tracers. A Panasonic HC-V770 camera was positioned 2.8 m above the physical model, monitoring the plan view at a rate of 25 frames per second with a resolution of 1920 px by 1080 px. The time-averaged surface velocities estimated by the LSPIV technique stabilized after different periods of time for the various areas of the model, but none of them exceeded 60 s (Mejia-Morales et al., 2021). More details about the seeding of the flow, the flow monitoring, the data post-processing, and a validation of the LSPIV measurements against measurements with an acoustic Doppler velocimeter (ADV) are provided in Mejia-Morales et al. (2021).

For the unsteady flow cases, it was not feasible to monitor the flow velocities in the whole flow area. Only the surface velocities within the porous block and at two points in the Right Street and Left Street (shown in Figure 1b) were monitored. Moreover, an ensemble average was not used for the LSPIV due to prohibitive post-processing load (Mejia-Morales et al., 2022a). A Sony ZV-1 camera with a sampling rate of 25 frames per second was used and the collected frames were averaged over periods of 2 seconds to filter the data.

### ***2.2.*** *Urban block configurations*

In every experiment, the urban block was in the same position near the downstream end in the $x$ direction and had the same dimensions $L_x$ and $L_y$ (Figure 1). However, the conveyance porosity (i.e., the porosity of each sidewall of the urban block), $\psi$, as defined by the number and locations of openings, differed in each experiment. Each opening had a width $L_{op}$ = 6 cm and each sidewall of the block had no more than three openings. In all tests, the water surface elevation remained lower than the height of the openings. In the present paper, three series of configurations for the porous block are examined (Figure 2):

- The first series comprises the eight configurations presented by Mejia-Morales et al. (2021) without obstruction within the block (Figure 2a). The conveyance porosity of each configuration is presented as C*xx*-*yy*, where *xx* and *yy* denote the ratio of the total length of the openings in a side of the porous block to the length of that side, in percent, in the $x$ and $y$ directions, respectively. The locations of the openings in the configuration with the largest conveyance porosity (C19-12) are shown in Figure 1a. The conveyance porosity in the rest of the configurations is determined by closing some of the openings of C19-12, while maintaining symmetry in the porous block openings.

- The second series comprises five new configurations, constructed and tested with the same experimental approach as Mejia-Morales et al. (2021), also without obstructions within the block (Figure 2b). The common trait of these configurations is that each configuration has four openings in its perimeter (the remaining ones after blocking eight openings in C19-12 shown in Figure 1a). Since there is no symmetry in every configuration, these configurations are simply named C1 – C5 in order of appearance.
- The configurations in the third series, presented in Mejia-Morales et al. (2022a), have one opening in the middle of each wall of the block and a non-porous rectangular obstacle in the center of the block. The footprint area of this obstacle was varied as shown in Figure 2c, leading to an areal porosity, $\phi$, for each case that is determined as the ratio of the empty area within the block to its total internal area.

Note that the concept of porosity is introduced here for the sole purpose of providing a macroscopic description of the considered geometric layouts (Figure 2), while the flow models used in this study are not porosity shallow-water models (e.g., Dewals et al. (2021)) . They aim to fully resolve the flow field on the considered computational mesh.

The first and second series were used with steady flow conditions, while the third series was used with both steady and unsteady flow conditions. Details about the upstream boundary conditions of each case are presented in Section 2.4.

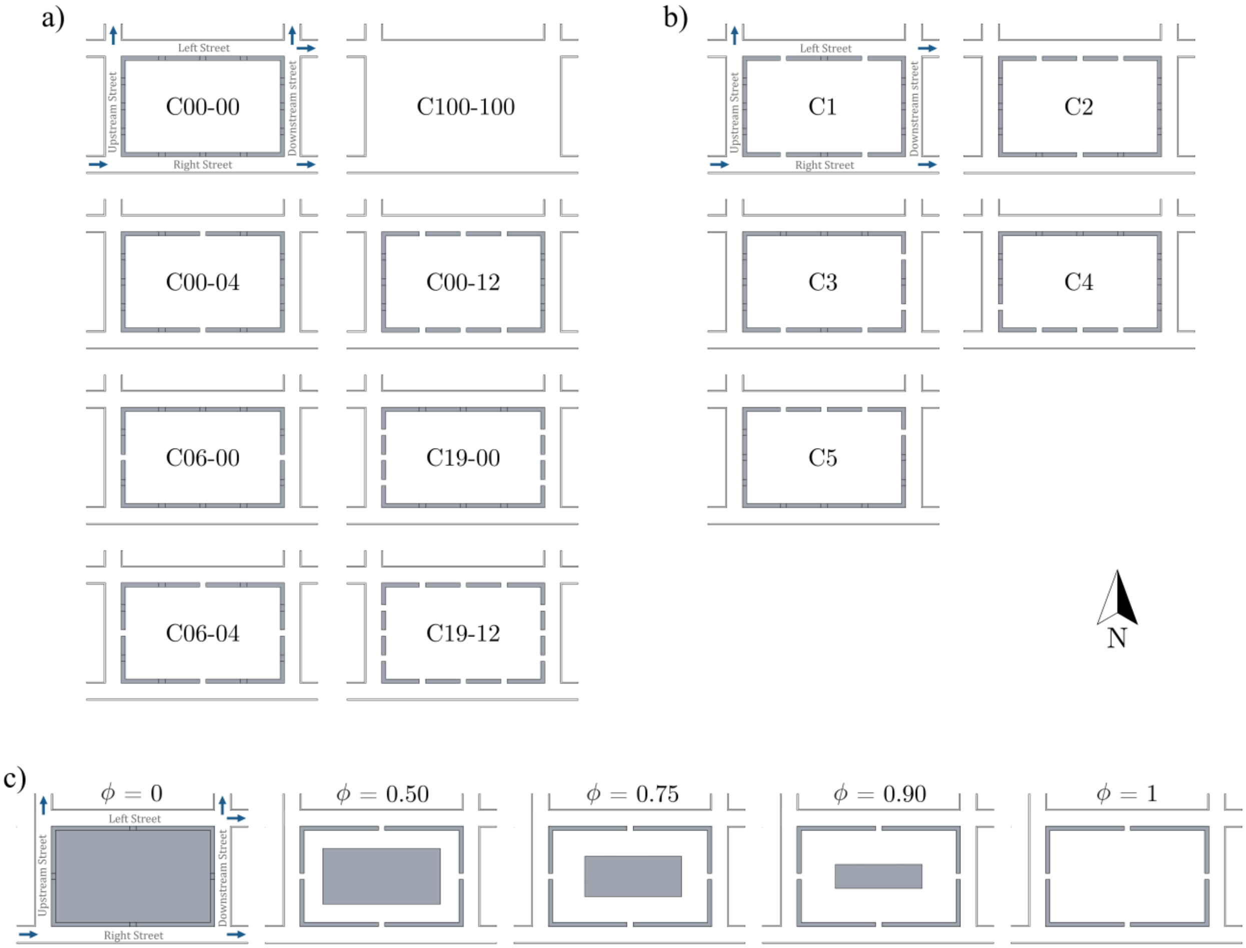


**Figure 2.** (a) Geometric configurations of the porous block of Mejia-Morales et al. (2021) with steady flow (series 1), (b) new geometric configurations of the porous block with steady flow (series 2), and (c) geometric configurations of the porous block with steady and unsteady flow (series 3). The arrows in the first geometric configuration of each subfigure show the flow direction in each street around the porous block and they are the same for the rest of the geometric configurations in each subfigure. In (a), the conveyance porosity, $\psi$, of each sidewall of each configuration is given by C*xx*-*yy*, where *xx* and *yy* denote the $\psi$ value in percent in the $x$ and $y$ directions, respectively. In (b), due to lack of symmetry in every case, the naming of the configurations is simply in order of appearance. In (c), the symbol $\phi$ denotes the areal porosity of the porous block as defined by the ratio of the empty space within the block to its total internal area. The grey rectangles in the center of the blocks in subfigure (c) denote solid non-porous obstacles. The blocks in (a) and (b) were tested in the experimental setup of Figure 1a and the blocks in (c) were tested in the experimental setup of Figure 1b.

The physical models were designed by assuming a geometrically distorted scale, with horizontal and vertical scale ratios equal to 50 and 10, respectively. This means that a studied flow in the physical model may be interpreted as a representation of a real-world flow in streets with 7.5 m in width around an urban block with dimensions 78 m × 48 m and openings 3 m wide. The upscaled studied flow depths are around 60 cm. This approach ensures relatively large depths in the physical model to enable a satisfactory measurement accuracy (Heller, 2011; Li et al., 2021b).

## *2.3. Numerical modelling*

The laboratory experiments were simulated using two academic numerical codes that solve the 2D SWE equations. The two models have differences in their mathematical formulation and their numerical discretization. The first model is implemented in the software Rubar20 (Mignot et al., 2008) developed by the Riverly research unit of Inrae in Lyon and the second one is implemented in Wolf 2D (Erpicum et al., 2009) developed by the HECE group at the University of Liege. Table 1 provides an overview of the characteristics of each model, referred to as Model 1 for Rubar20 and Model 2 for Wolf 2D. The steady flow cases were simulated with both numerical models, while only Model 1 was used for the simulation of the unsteady flow cases.

**Table 1.** Details of the tested numerical models.

| | Model 1 | Model 2 |
|---|---|---|
| Software | Rubar 20 | Wolf 2D |
| Reference | Mignot et al. (2008) | Erpicum et al. (2009) |
| Turbulence closure | Elder's formula (zero-order model) | Depth-averaged $k$-$\varepsilon$ model |
| Friction formula | Explicit Colebrook-White (Yen, 2002) (Eq. (7)) | Colebrook-White (Eq. (6)) |
| Numerical scheme | Godunov type | Flux-vector splitting |

### *2.3.1. Governing equations*

The two codes solve the conservative form of the 2D SWE, which means that the main unknowns are the flow depth, $h$, and the specific discharges, $hu$ and $hv$, with $u$ and $v$ denoting the depth-averaged flow velocities along the $x$ and $y$ direction, respectively. The 2D SWE in conservative form are formulated as in Eqs. (1)-(3) (Wu, 2008):

$$\frac{\partial h}{\partial t}+\frac{\partial hu}{\partial x}+\frac{\partial hv}{\partial y}=0 \tag{1}$$

$$\frac{\partial hu}{\partial t}+\frac{\partial}{\partial x}\left(hu^2+\frac{gh^2}{2}\right)+\frac{\partial huv}{\partial y}=\frac{\tau_{bx}}{\rho}+\frac{1}{\rho}\frac{\partial h\tau_{xx}}{\partial x}+\frac{1}{\rho}\frac{\partial h\tau_{xy}}{\partial y} \tag{2}$$

$$\frac{\partial hv}{\partial t}+\frac{\partial huv}{\partial x}+\frac{\partial}{\partial y}\left(hv^2+\frac{gh^2}{2}\right)=\frac{\tau_{by}}{\rho}+\frac{1}{\rho}\frac{\partial h\tau_{xy}}{\partial x}+\frac{1}{\rho}\frac{\partial h\tau_{yy}}{\partial y} \tag{3}$$

where $g$ is the acceleration of gravity, $\rho$ is the water density, $t$ is the time, $\tau_{xx}$, $\tau_{yy}$, and $\tau_{xy}$ are the depth-averaged stresses comprising both the Reynolds and molecular stresses (Erpicum et al., 2009), and $\tau_{bx}$ and $\tau_{by}$ are the bed shear stresses in the $x$ and $y$ direction, respectively, calculated from Eqs. (4) and (5) in line with Camnasio et al. (2014):

$$\frac{\tau_{bx}}{\rho}=f\frac{u\sqrt{u^2+v^2}}{8} \tag{4}$$

$$\frac{\tau_{by}}{\rho}=f\frac{v\sqrt{u^2+v^2}}{8} \tag{5}$$

where $f$ is the Darcy-Weisbach bed friction coefficient.

The Darcy-Weisbach formulation is used in both models, but the friction coefficient $f$ of the bottom and side-walls is estimated by the Colebrook-White formula (Eq. (6)) (Idel'cik, 1969) in Model 2 and by its explicit equivalent formula (Eq. (7)) (Yen, 2002) in Model 1.

$$\frac{1}{\sqrt{f}}=-2\log\left(\frac{k_s}{14.8h}+\frac{2.51}{\mathrm{Re}\sqrt{f}}\right) \tag{6}$$

$$f=\frac{1}{4}\left[-\log\left(\frac{k_s}{12h}+\frac{6.79}{\mathrm{Re}^{0.9}}\right)\right]^{-2} \tag{7}$$

where $k_s$ is the roughness height and Re is a Reynolds number $\mathrm{Re} = 4\sqrt{u^2 + v^2}h/\nu$ with $\nu$ the kinematic viscosity of water.

Although both models were derived by depth-averaging the Reynolds-averaged Navier-Stokes equations, together with Boussinesq's assumption for expressing the depth-averaged turbulent stresses, they differ by the type of turbulence closure used. Model 1 is based on a zero-order turbulence closure, in which the eddy viscosity, $\nu_t$, is estimated by Elder's formula: $\nu_t = \lambda h u_*$, with $u_*$ the friction velocity computed from the free surface slope and $\lambda$ a parameter set by the user with a default value of 1 (Mejia-Morales et al., 2020). In Model 2, a second-order turbulence closure is implemented. It consists in a two-length-scale depth-averaged $k$-$\varepsilon$ turbulence model, as detailed by Erpicum et al. (2009) and Camnasio et al. (2014).

#### ***2.3.2.****Numerical discretization*

In both models, the computational domain was meshed with a Cartesian square grid aligned with the street sidewalls. Depending on the model run, the grid spacing, Δx, was varied between 5 mm and 30 mm with the resulting ratio of the grid size to the length of one opening in the porous block, $L_{op}$, ranging from 1/2 to 1/12. Both models are solved with a finite volume technique. In Model 1, a Godunov type scheme is used (Mignot et al., 2008), while Model 2 is based on a flux-vector splitting technique (Erpicum et al., 2010). In both models, the variables at the cell edges are evaluated from a linear reconstruction, achieving second-order accuracy in space. For steady flow calculations, the models are run in unsteady mode until a steady state is reached. The time step used in the simulations is of the order of $10^{-3}$ seconds, as it is constrained by the Courant-Friedrichs-Lewy (CFL) stability condition. In both models, the CFL number was set at 0.5. The computational time necessary to reach convergence towards a steady-state varied with the considered geometric configuration and initial conditions. It was generally of the order of an hour on a standard desktop.

### *2.4. Boundary and initial conditions*

The computational domain was delimited by three types of boundaries: sidewalls, inlets, and outlets. At each sidewall, the component of the specific discharge normal to the sidewall was set to zero. At the inlets, the specific discharge in the streamwise direction was prescribed, and the normal component of the specific discharge was set to zero. The two inlets that are considered in the Left Street and Right Street were positioned at a distance of 2.94 m upstream of the uppermost street intersections (Figure 1), i.e., at the location of the honeycomb grid at the entrance of each street in the experiments.

For the steady flow cases in the first and second series of tests (Figure 2a and b), steady inflow discharges were prescribed: $Q_{\mathrm{in}_1} = 4.5$ l/s and $Q_{\mathrm{in}_2} = 2.0$ l/s (Figure 1) in consistency with the measured values. For the unsteady flow cases in the third test series (Figure 2c), the inflow discharge was fed only through the Right Street as a sequence of 50 consecutive identical flood waves. Three different floodwaves were tested (Figure 3) and each one was examined separately. Each floodwave had the same peak flow of 5 l/s (Figure 3) but was characterized by a different unsteadiness degree (Mejia-Morales et al., 2022a). The floodwaves were distinguished based on the rising discharge time, the falling discharge time, and the total volume of floodwater, while their names were formed by using an “L” or an “S” for large and small magnitude for each one of the floodwave characteristics, respectively. For example, H.LSS denotes a hydrograph with large rising discharge time, small falling discharge time, and small total volume of floodwater. As a reference case, steady flow experiments with inlet discharge of 5 l/s (i.e., equal to the peak of the floodwaves) through the Right Street were also carried out in the geometrical setup of test series 3 (Figure 1b with the urban blocks of Figure 2c).

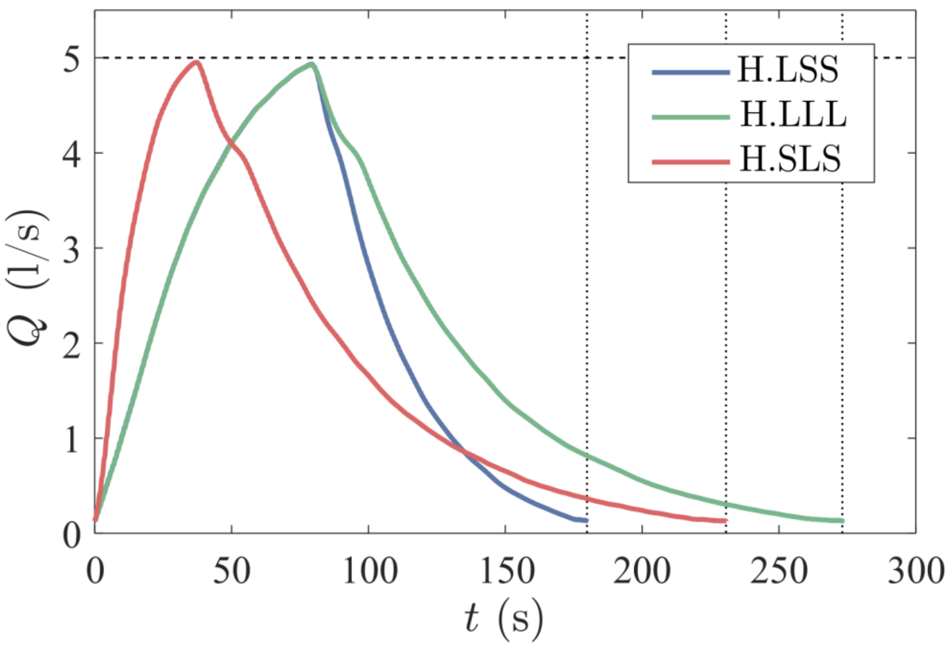


**Figure 3.** Unsteady hydrographs used as inlet discharge in the Right Street (Figure 1b) for the porous blocks of Figure 2c.

At the outlets, the outflow discharge was prescribed as a function of the computed flow depth. The outlet boundaries were positioned as follows (Figure 1):

- in the Right Street and the Left Street, at a distance of 0.6 m downstream of the easternmost street intersection.
- in the Upstream Street and the Downstream Street, at 1.94 m downstream of the northernmost street intersection.

For test series 1 and 2 (Figure 2a and b), the outflow discharge, $Q_0$, in each outlet was determined from the following weir formula (e.g., Roger et al. (2009)):

$$Q_0 = LC_D\sqrt{2g(h-w)^3} \tag{8}$$

where $L$ is the weir length, $C_D$ is the discharge coefficient, and $w$ is the weir height.

The implementation of Eq. (8) is slightly different in the two models:

- in Model 1, the value of $L$ is set equal to the mesh size, and distinct values of $Q_0$ are computed at each cell edge along the outlet boundary as a function of the flow depth computed at the relevant cell;
- in Model 2, the length $L$ is taken equal to the actual weir length (i.e., the street width $b$) and a single value of $Q_0$ is evaluated, assumed uniformly distributed over the weir length, as a function of the average of the computed flow depths over the cells next to the outlet boundary.

For test series 3 (Figure 2c), the downstream boundary condition was set to critical flow for all the edges of an outlet because the flow goes directly from the street to the outlet tank without a weir.

In the steady flow runs of Model 2, the initial condition was either a converged solution from a previous run or a calm body of water with an initial flow depth equal to 0.05 m. For Model 1, the initial condition for the steady flow calculations was a water level close to the experimental value and for the unsteady flow calculations was zero flow depth across the flow domain.

## 3. Results and discussion

### *3.1. Sensitivity analysis and calibration of the numerical models*

Model 2 was used systematically in a series of preliminary computations to assess the effect of the variation in the (i) grid spacing, Δx, (ii) roughness height, $k_s$, (iii) discharge coefficient, $C_D$, of the weirs at the outlets, and (iv) initial conditions. Model 1 was also used in these preliminary computations, but not in a systematic way. Moreover, Model 1 was used to verify whether considering a theoretical bottom topography (flat bed) instead of the real one influences the results. These sensitivity analyses were conducted for a single geometric configuration (C19-12 in Figure 2a), which includes the largest number of openings and leads to the most complex flow fields. The comparison of the computed, $y_i^c$, and observed, $y_i^o$, hydraulic variables was carried out based on the bias and the root mean square error (RMSE) (e.g., Chen et al. (2010)):

$$\text{bias} = \frac{\sum_{i=1}^{N}(y_i^c - y_i^o)}{N} \tag{9}$$

$$\text{RMSE} = \sqrt{\frac{\sum_{i=1}^{N}\left(y_i^c - y_i^o\right)^2}{N}} \tag{10}$$

where $N$ is the number of points where both measured and modelled data were available.

### *3.1.1. Grid spacing*

The grid cell size for Model 2 was selected after repeating the computations for C19-12 three times with all parameters being kept the same except the grid cell size. The three mesh grids that were tested had square grid cells with side length, $\Delta$, equal to 30 mm, 10 mm, and 5 mm, respectively. The bias and RMSE of the flow depths and velocities for different areas of the model were significantly reduced when the grid cell size was reduced from 30 mm to 10 mm but did not vary much when the cell size was further reduced from 10 mm to 5 mm (Figure S1a in the Supplementary Material). Figure S1a in the Supplementary Material also confirms the second order accuracy of the finite volume numerical scheme implemented in Model 2, consistently with the linear reconstruction used in this model.

However, the features of the simulated flow velocity patterns (i.e., number and size of recirculating flow areas) within the porous block were more consistent with the features of the measured patterns when the cell size was 5 mm (Figure S2a in the Supplementary Material), even though some flow recirculations were not captured entirely. Therefore, the 5 mm cell size was kept for the rest of the analyses with Model 2. The number of cells is close to 160,000, and it varies slightly depending on the geometric configuration (number of openings).

Model 1 exhibited similar behavior with Model 2 when varying the cell size with the rest of the parameters being kept the same, however, with Model 1 the flow velocity patterns were similar for mesh sizes of 10 mm and 5 mm (Figure S3a in the Supplementary Material). Thus, to reduce computational times, the 10 mm mesh was kept for the rest of the analyses with Model 1, leading to about 40,000 cells.

With these mesh configurations, the computed flow depths exhibited a systematic bias compared to the observations, which motivated the extension of the sensitivity analysis to the roughness height and the discharge coefficients of the weir outlets.

*3.1.2. Roughness height*

The roughness height was taken at a small value corresponding to the PVC surface of the laboratory model. The tested values of $k_s$ were equal to $2 \times 10^{-4}$ m, $8 \times 10^{-5}$ m, and $3.6 \times 10^{-5}$ m. This sensitivity analysis was conducted with Model 2, with $\Delta x$ = 5 mm and $C_D$ = 0.527 for all outlets, with a previously converged flow field as initial condition. The three tested values for the roughness height did not affect significantly the flow depths and velocities results (Figure S1b in the Supplementary Material) nor the flow patterns (Figure S2b in the Supplementary Material). The flow depth bias and RMSE values for the lowest value of $k_s$ were slightly lower compared to the other $k_s$ values, but at the same time the flow velocity bias and RMSE values slightly increased. The $k_s$ value of $3.6 \times 10^{-5}$ m was calibrated from water surface measurements in a single street without openings. Considering the very small influence of the tested $k_s$ values on the simulated results with Model 2, a similar sensitivity analysis was not repeated with Model 1 and $k_s = 3.6 \times 10^{-5}$ m was used in both models.

*3.1.3. Discharge coefficient of the weirs*

The computations presented in Section 3.1.1 used discharge coefficients that were experimentally derived from the laboratory tests. However, the location where the flow depth is measured upstream of the weirs in the lab does not correspond exactly to the location where the Model 2 considers flow depth for estimating the outflow discharge. Hence, the discharge coefficient, $C_D$, which lumps all flow processes in the near field of the weirs (including vertical acceleration, which cannot be represented explicitly by shallow water equations) was recalibrated so that the computed flow depths agree on average with the observations. To this end, several values of $C_D$ were tested. The lowest difference between modelled and measured flow depths for Model 2 was obtained with $C_D = 0.453$, and thus this value was selected for the rest of the numerical simulations using Model 2. For Model 1, the lowest difference between modelled and measured flow depths was obtained with $C_D = 0.467$ and this value was chosen for the rest of the simulations with Model 1, although a value of 0.55 for Outlets 1 and 2 and 0.53 for Outlets 3 and 4 led to a better distribution of the outflows. This was also the case for all the urban blocks in Figure 2a. Nevertheless, the effect of $C_D$ on the street and block intrusion discharges and on the flow patterns (Figure S2c and Figure S3b in the Supplementary Material) is rather small. The small difference between the chosen discharge coefficients for the two models may be attributed to the different ways that the downstream boundary conditions were implemented in the models and to the different turbulent closures.

#### *3.1.4. Initial conditions*

A converged solution for a steady flow simulation may depend on the initial conditions (Dewals et al., 2012), particularly in the presence of complex patterns of recirculating flow. Therefore, by using Model 2 for the case with the C19-12 block (Figure 2a), we repeated the computations for two different initial conditions: (i) the computed steady flow field obtained with the experimentally derived discharge coefficient (i.e., a previously converged solution) and (ii) water at rest with flow depth equal to 5 cm. As expected, the initial condition influenced the computed steady flow field. For the flow in the porous block, the results obtained when the computations were initiated with water at rest agree better with the observations (Figure S1c and Figure S2d in the Supplementary Material). This initial condition setting was kept for the rest of the analysis for Model 2 while the initial condition for Model 1 was a water level close to the experimental value. For Model 1 the results were generally independent of the initial conditions, but exceptions could be found for the more complex patterns inside the block.

The simulation parameters obtained from the sensitivity analysis are summarized in Table 2 and these parameters were used for the numerical modelling of the rest of the experimental configurations.

**Table 2.** Calibrated parameters used for the numerical modelling of all cases.

| | Model 1 | Model 2 |
|---|---|---|
| Cell size, $\Delta x$ | 10 mm | 5 mm |
| Initial conditions | Water level close to experimental value | Water at rest |
| Roughness height, $k_s$ | $3.6 \times 10^{-5}$ m | $3.6 \times 10^{-5}$ m |
| Outlet weirs discharge coefficient, $C_D$ | 0.467 | 0.453 |

#### *3.1.5. Topography*

The topography of the experimental platform may change in time since it was constructed with boards supported by beams. For most numerical calculations, the theoretical topography of an inclined plane with a constant slope in the $x$ direction of 0.12% was used. However, two detailed topographies that were surveyed in 2019 (before the first series of experiments, i.e., Figure 2a) and in 2021 (between the second and third series of experiments, i.e., Figure 2b and Figure 2c, respectively) showed some elevation differences compared to the theoretical topography, and between the two topographical surveys, of less than 2 mm. The effect of this change in topography was tested using Model 1 and $C_D$ = 0.4. Results show a weak influence on the flow velocity pattern and all the other results (Table S1 in the Supplementary Material), thus, the theoretical topography was used for the rest of the cases.

### *3.2. Steady flow tests*

#### *3.2.1. Flow depths*

Figure 4 shows that both models, and hence the 2D SWE, are able to reproduce fairly accurately the measured flow depth patterns for cases with steady flow (Figure 2a and b). There is a flow depth difference between the Right and Left Streets because the weir height in Outlet 1 is larger than in Outlet 2. The larger flow depths in the Right Street compared to the Left Street induce a pressure gradient that enhances the transverse flow through the porous block openings.

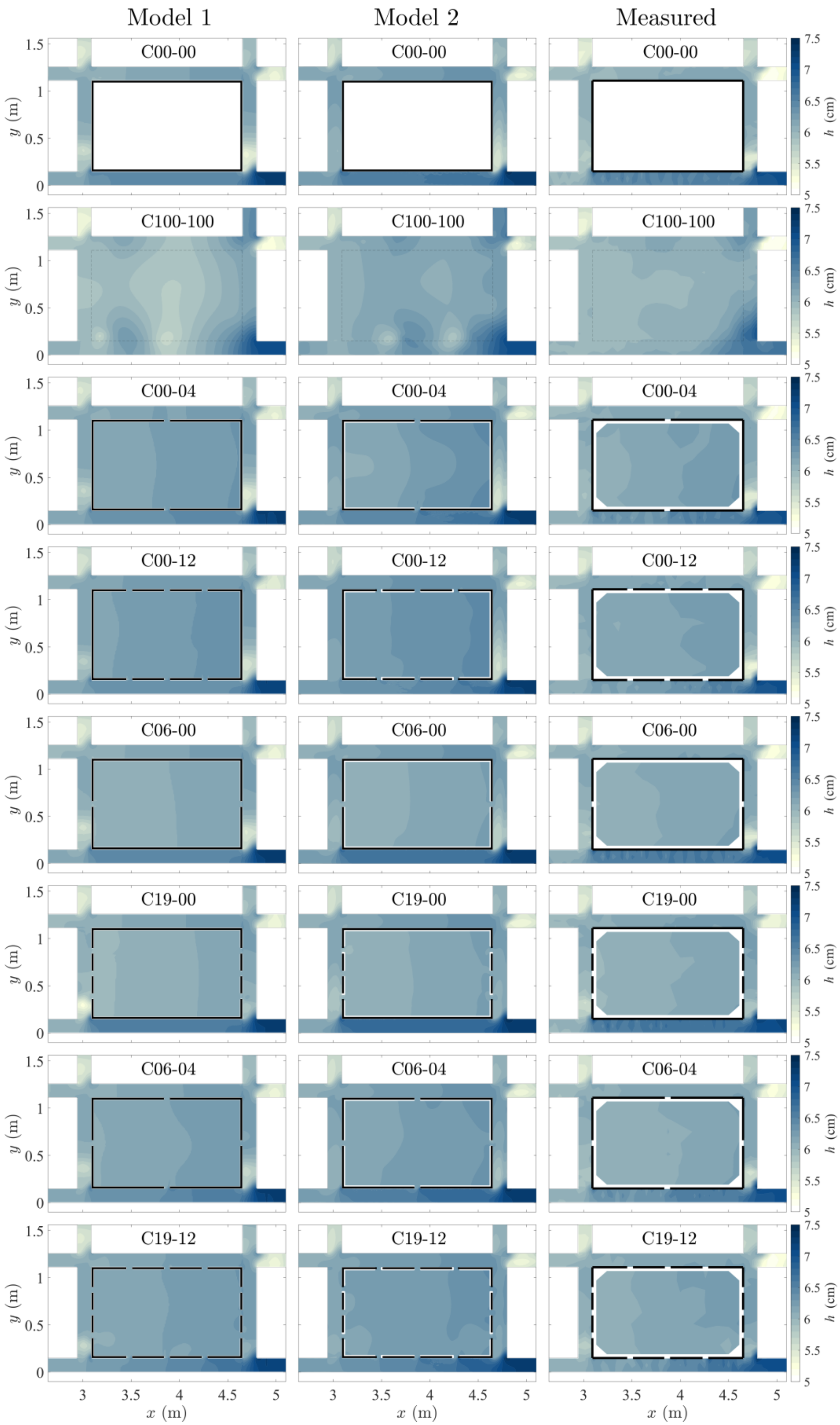
Model 1
Model 2
Measured
C00-00
C100-100
C00-04
C00-12
C06-00
C19-00
C06-04
C19-12
y (m)
x (m)
h (cm)


485

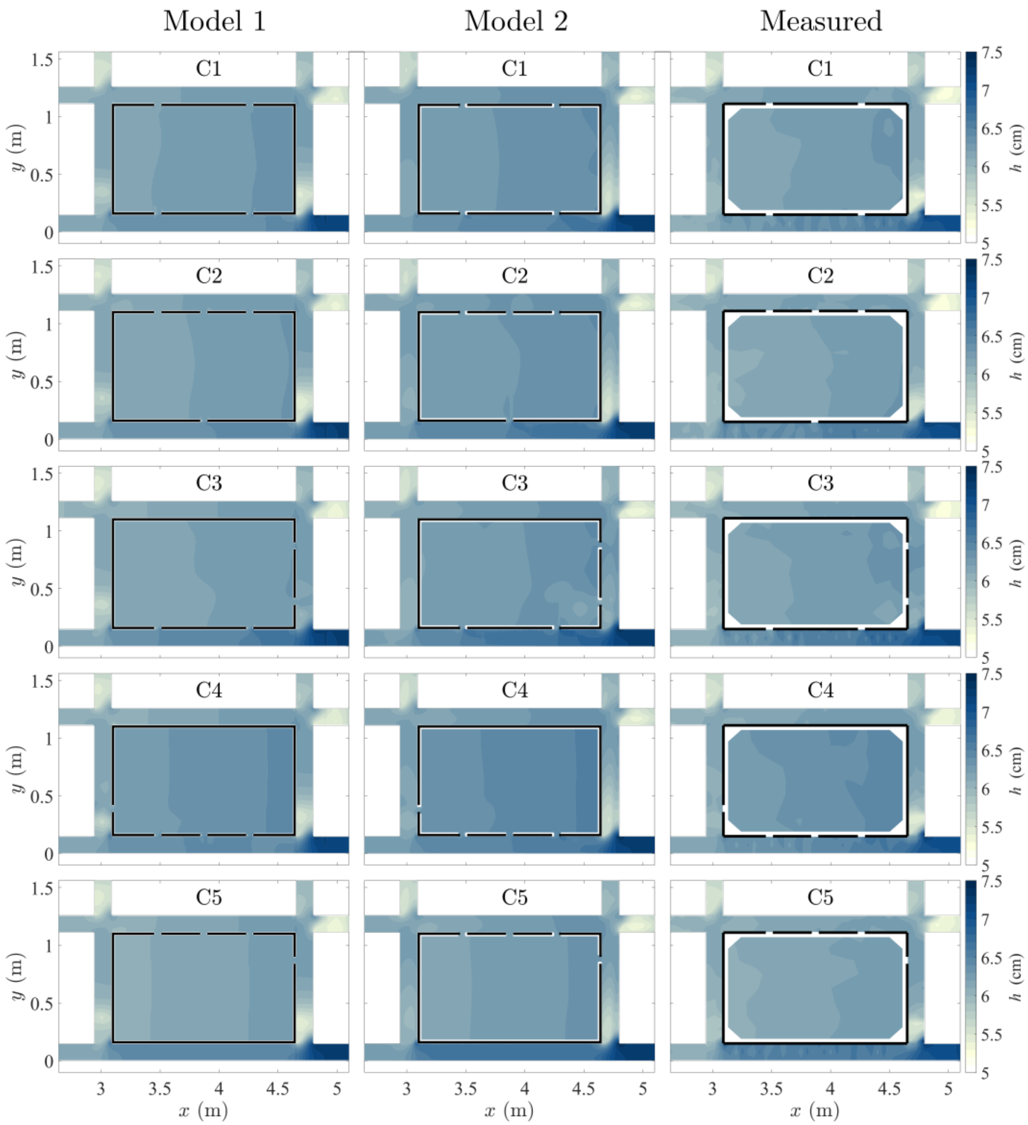


**Figure 4.** Flow depths modelled with Model 1 (left column), Model 2 (middle column) and measured (right column) for steady flow conditions. The first eight configurations are from Mejia-Morales et al. (2021).

Both models are capable to reproduce the increasing flow depth at the Right Street, the decreasing flow depth at the Left Street, and the relatively constant water level within the block, which is a result of the very low velocities within the block. The differences between the results of the two models are minimal both within the porous block and in the streets, which implies that at a large scale the turbulence closure model does not affect the flow depth predictive capabilities of a 2D SWE model in urban floods with steady flow.

### *3.2.2. Discharge partition*

The two models reproduce well the discharge partition both in the streets and within the porous block without any of the two exhibiting clearly superior performance (Figure 5a). Model 1 predicts more accurately the discharge partitioning at the four outlets with a RMSE that is less than half of that of Model 2 (Figure 5c). Model 2 overestimates $Q_{\mathrm{out}_4}$ and both models underestimate $Q_{\mathrm{out}_1}$, except for the case C100-100 (configuration without a block), and approximate well $Q_{\mathrm{out}_2}$ (Figure 5b). The two models exhibit a different behavior in Outlet 3, with Model 1 overpredicting and Model 2 underpredicting $Q_{\mathrm{out}_3}$ (Figure 5b). Overall, Model 1 and Model 2 miscalculate the discharge distribution at the outlets by 2.5% and 7.3% on average, respectively. In the streets surrounding three of the most complex porous blocks (C06-04, C19-12, C3), Model 2 overestimates the discharge in the Right Street, which is the street that conveys most of the discharge, while Model 1 exhibits a more erratic pattern with this discharge (Figure 6). The street that conveys the second largest discharge in these three cases is the Downstream Street, in which both models give good results, besides Model 2 overpredicting the discharge in C19-12. The overpredictions of Model 2 and underpredictions of Model 1 at the large discharges in the Right and Downstream Streets are partially compensated by respective underpredictions and overpredictions of the two models at the street with the smallest discharge, i.e., the Upstream Street (Figure 6). The discharge distribution for all cases is presented in Figure S4 in the Supplementary Material. Overall, the maximum discharge deviation occurs for C100-100 (Figure 5c). Similar disagreements between measurements and 2D SWE computations in large open areas were also noted by Li et al. (2021a).

Generally, the flow distribution at the outlets corresponds to the experimental ones (error less than 2.5% of the total inflow except the case C100-100) but this distribution is relatively constant due to the general configuration of the street network. Flow discharges in the streets and through the openings of the block are more influenced although the RMSE remains below 2% of the total discharge. However, due to the small portion of the flow that enters the block, the relative error can be high for the flow passing through the building (Figure S4 in the Supplementary Material).

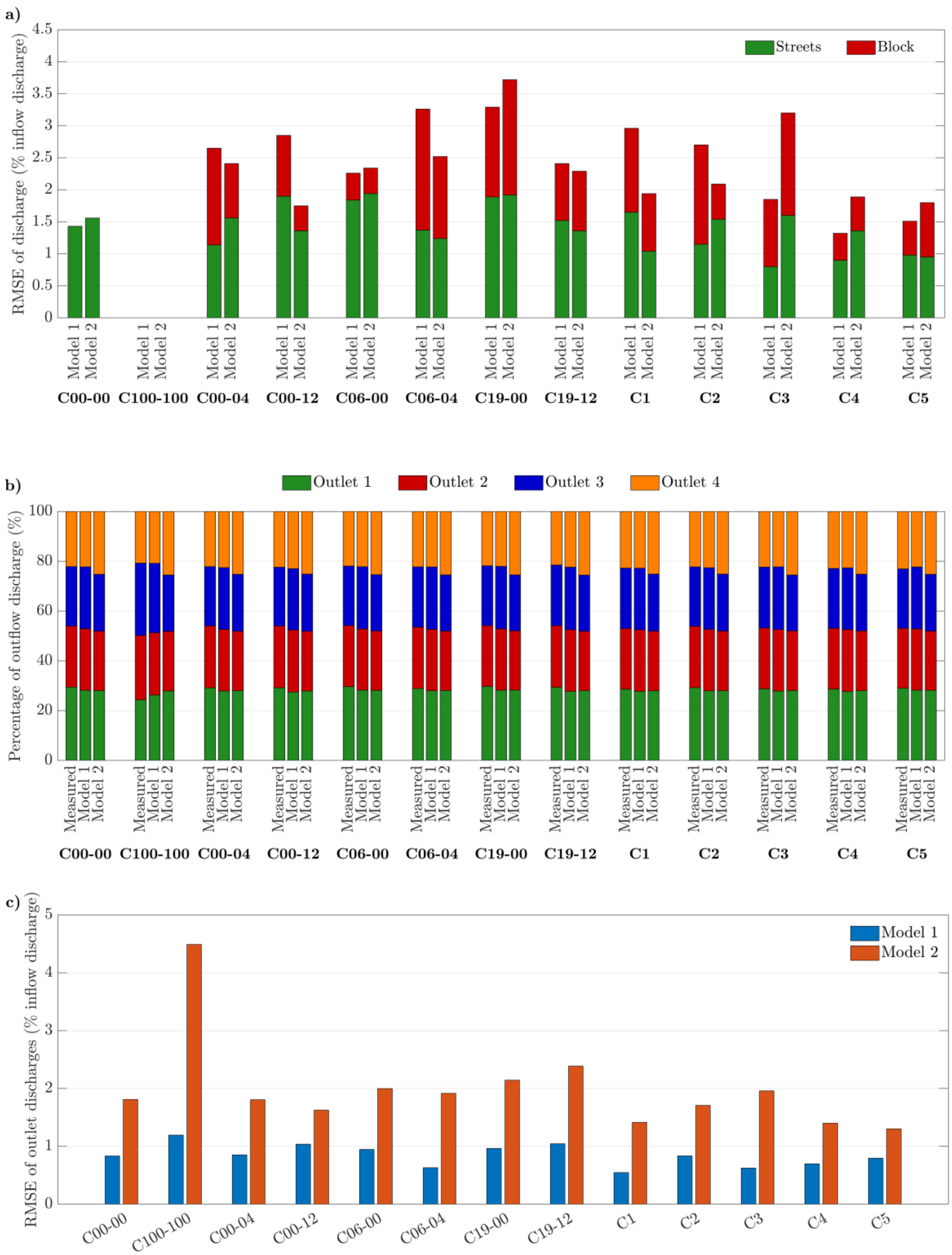


**Figure 5.** (a) RMSE of flow discharge for Model 1 and Model 2 in the urban block and in the surrounding streets, (b) Discharge distribution at the four outlets and (c) RMSE between modelled and measured outlet discharges at the four outlets for the steady flow cases. No data are presented for C100-100 in (a) because this case does not have a block.

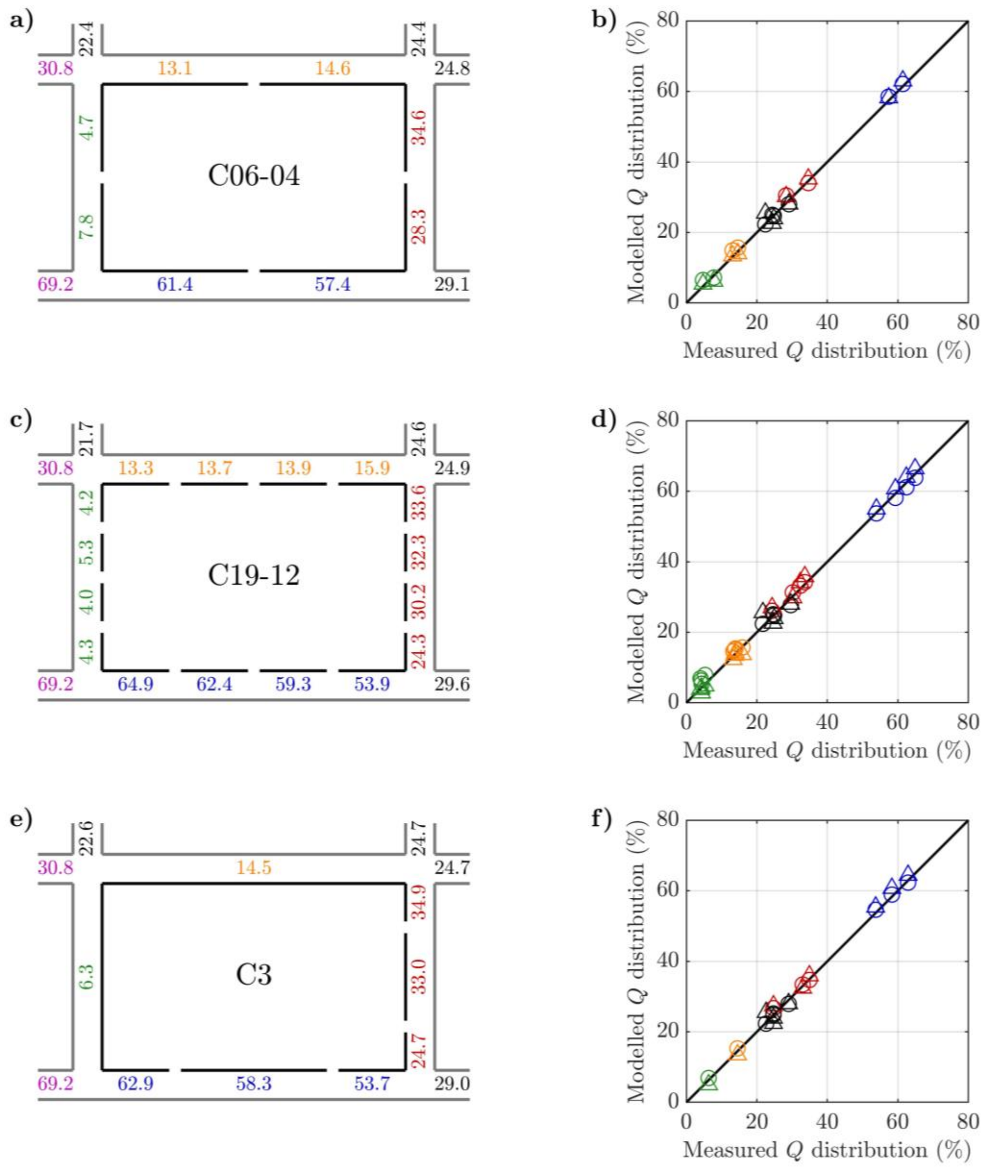


**Figure 6.** (a, c, e) Measured discharge distribution around the urban block and at the outlets for selected cases with steady flow conditions and (b, d, f) comparison between measured and modelled discharges with Model 1 (circles) and Model 2 (triangles). The colored symbols in each scatter plot of the right column correspond to the discharges with the same color in the subfigure next to each scatter plot in the left column.

*3.2.3. Velocity flow fields*

In this section, the depth-averaged flow velocities modelled with 2D SWE are compared to the surface velocities measured with LSPIV. Mejia-Morales et al. (2021) compared the LSPIV surface velocity measurements to ADV measurements across the flow depth and showed that the surface velocities are mostly well-approximated by depth-averaged velocities. Starting with the two reference cases C00-00 (non-porous block) and C100-100 (no block), the two models reproduce qualitatively all the flow features that were observed in the experiments (Figure 7). In C00-00, the interaction of the flows from the different branches at the junctions matches the measurements well, with a correct distribution of the discharge between the outlets (Figure 5c). In C100-100, even though the modelled discharge distribution at the outlets exhibits the largest deviation from the measurements (Figure 5c), the two models reproduce fairly well, particularly Model 2, the two large recirculation zones. However, they are uneven compared to the measurements, with the downstream and upstream recirculation zones being modelled larger and smaller, respectively, than what was observed.

The modelled flow patterns within and around the porous blocks in the first test series (Figure 2a) agree well with the measurements, with the number and direction of the recirculation zones being modelled correctly in almost all cases (Figure 7). For the cases with no more than one opening per side, i.e., C00-04, C06-00, and C06-04, only Model 2 in C06-04 exhibits a notable difference in the size of the recirculation zone in the lower left corner. When there are three openings at two opposite sides of the porous block, the flow pattern becomes much more complex. The two models are still able to simulate the direction of the streamlines quite correctly but the sizes of some of the recirculation zones are a little different than the measured ones. For C00-12, Model 1 adds two small recirculation zones at the right part of the block and Model 2 augments one in the center.

The second test series of steady flow cases (presented in Figure 2b) generally exhibits complex flow recirculations (Figure 7) because of the several openings on one side of the block, in each case, and the asymmetric distribution of the other openings at another side of the porous block. The case C1 is the only exception in the sense that it has two symmetric openings at the sides at the Right Street and Left Street. However, the flow pattern within the block for C1 is quite complex with three main uneven recirculation zones that the two models cannot reproduce in their correct location; moreover, the two models do not obtain the same pattern. In case C2, from the three openings at the Left Street, the middle one influences the flow pattern the most and the flow pattern in the porous block resembles C00-04. The two models reproduce this pattern accurately. Cases C3 to C5 are the more complex ones and the two models are not always able to reproduce entirely the observed flow patterns. The left part of the pattern in C3 is generally well reproduced by Model 1 but the right part with an interaction of three openings is not similar to the measurements. On the other hand, Model 2 predicts quite accurately the flow pattern in C3. Case C4 is the most challenging one: the two models provide similar patterns but fail to accurately predict the shape and size of the recirculation zones. As a result, the two observed large counter-rotating recirculation zones are modelled as one and the two smaller ones next to the Right Street have the opposite directionality. The structure of the smaller recirculation zones from the models seems more influenced by the opening at the Upstream Street, compared to the measurements. On the contrary, in a mirrored configuration, the modelled flow patterns in C5 (relatively similar for the two models) seem less influenced by the opening in the Downstream Street compared to the measurements, and as a result the recirculation zone at the right side of the block is modelled larger than what it actually is.

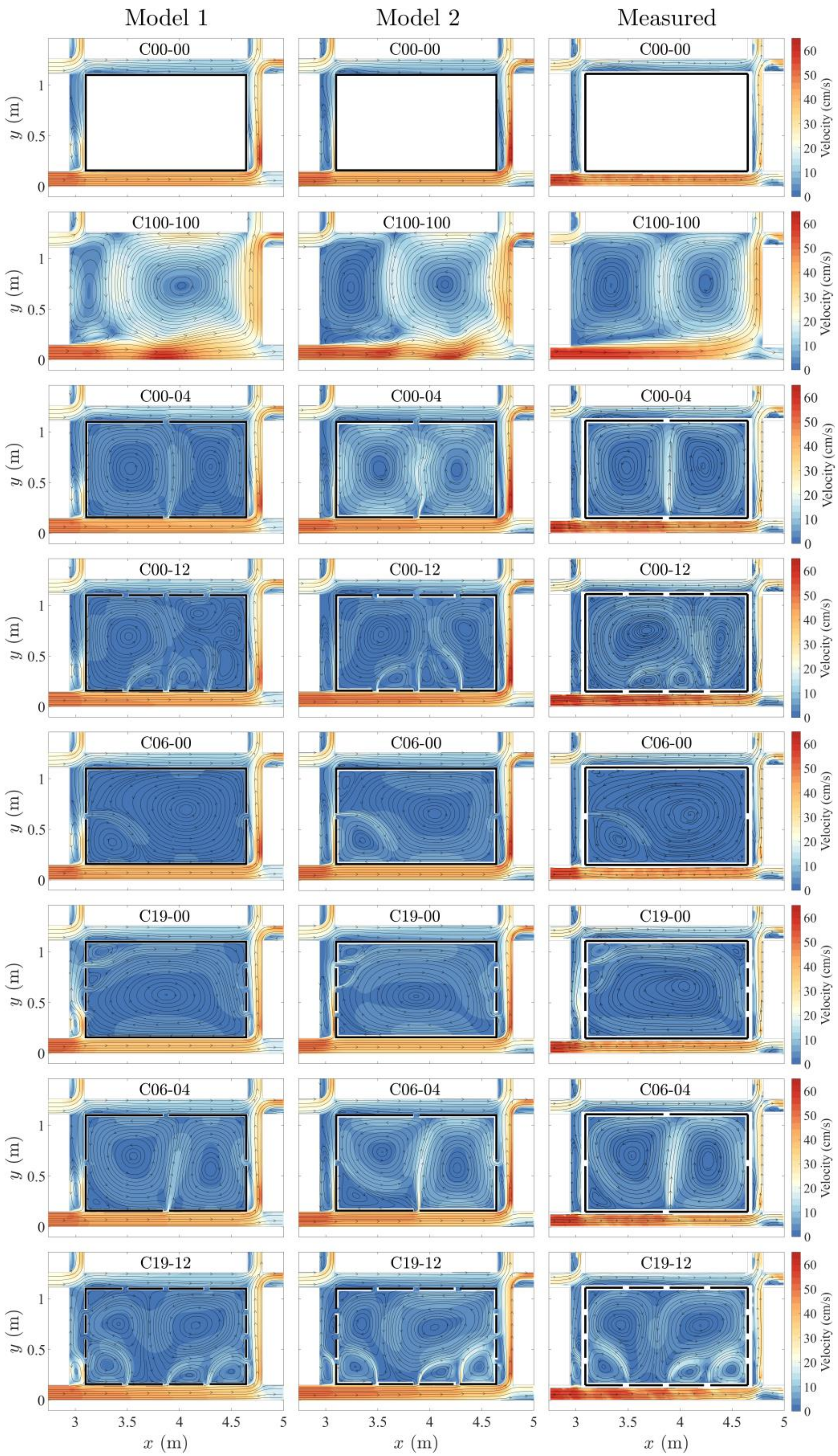
Model 1
Model 2
Measured
C00-00
C100-100
C00-04
C00-12
C06-00
C19-00
C06-04
C19-12
y (m)
x (m)
Velocity (cm/s)
0
10
20
30
40
50
60
3
3.5
4
4.5
5
0.5
1

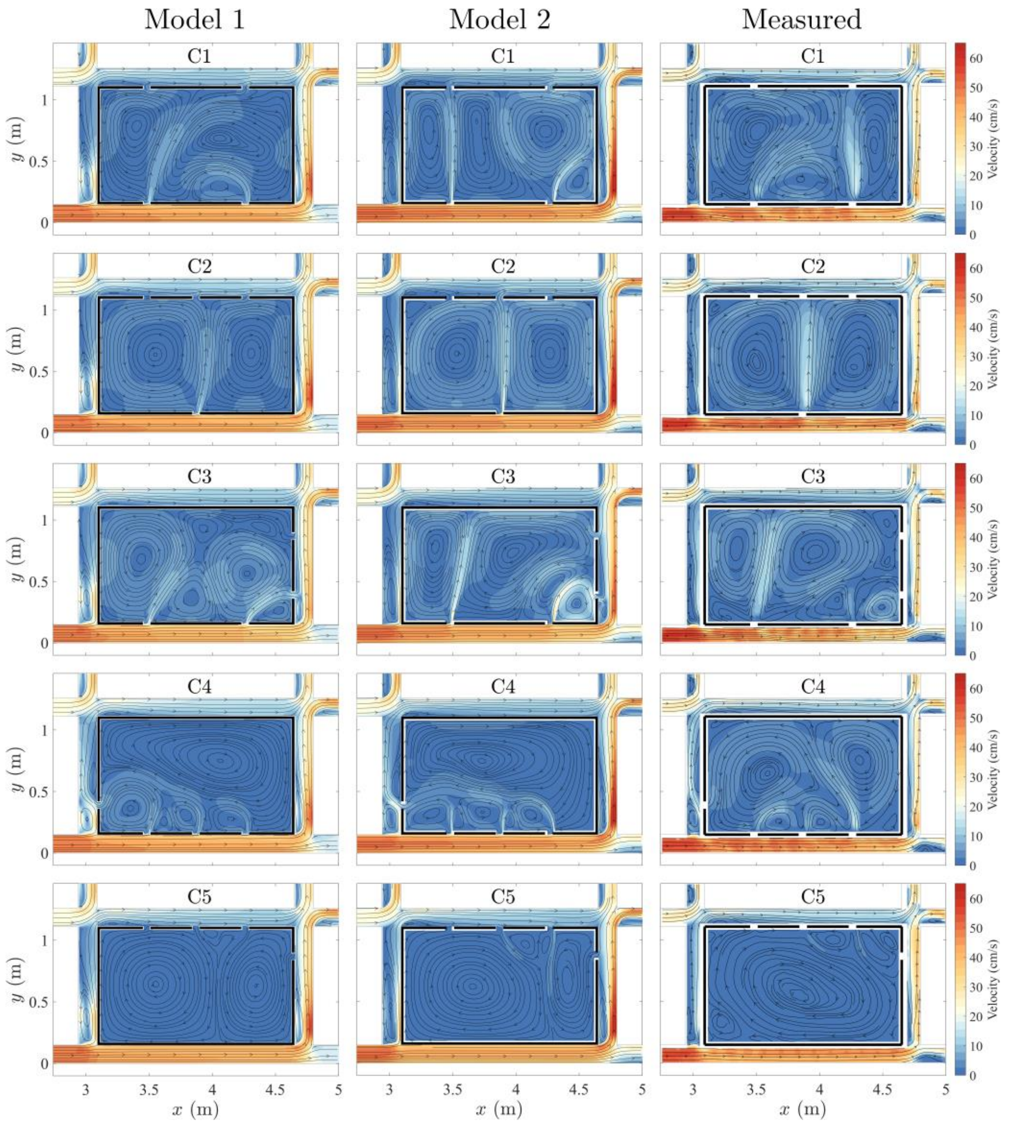


**Figure 7.** Time-averaged surface velocities modelled with Model 1 (left column), Model 2 (middle column) and measured (right column) for steady flow conditions. The first eight configurations are from Mejia-Morales et al. (2021). The modelled flow velocity patterns (left and middle columns) are based on depth-averaged velocities while the measured flow velocities are surface flow velocities.

### *3.2.4. Comparative analysis of the performance of Models 1 and 2*

The computational results reveal that both 2D models predict well the flow depths, with limited difference between the two models (Fig. 4). This is consistent with existing knowledge that the flow depth predictive capability of a 2D SWE model is little influenced by the turbulence closure, as multiple previous studies reported a good agreement between computed and observed flow depths while they used different approaches for the turbulence closure (Arrault et al., 2016; Bazin et al., 2017; Shettar and Murthy, 1996; Khan et al., 2000; El Kadi Abderrezzak et al., 2009).

The two models reproduce similarly well the experimentally observed discharge partition in the streets (Fig. 5a). In contrast, the considered error metrics suggest that the discharge partition at the outlets is better reproduced by Model 1 than by Model 2 (Figs. 5b and 5c). This may result from the difference in the implementation of the downstream boundary conditions between Models 1 and 2, as detailed in Section 2.4. Except in one configuration (C100-100), the differences between the computed and measured discharges do not exceed 2.5 % of the total inflow discharge. These differences should be set in perspective compared to the experimental uncertainties. The valve-flowmeter system used in the laboratory experiments have an error of 3 % of the measured flow rate (Mejia-Morales et al., 2021). Accordingly, the time convergence criterion used for the laboratory measurements was also set at 3 % (Mejia-Morales et al., 2021). Besides, the experimental method used to estimate the discharge in the streets requires assumptions to cover the blind zones near the boundaries (bed, walls, and free surface), as well as the inconvenience of using an intrusive instrument (ADV) in a narrow cross-section. This leads to an estimated error of 1.5% on average (Mejia-Morales et al., 2021). The maximum deviation between computed and observed discharges occurs for configuration C100-100 (empty central area). This is consistent with similar disagreements between measurements and 2D SWE computations in large open areas as reported by Li et al. (2021a).

Table 3 provides an overview of the agreement between the experimentally observed and computed flow fields by Models 1 and 2. The flow fields are visible in Fig. 7. The following observations can be made:

- In several configurations, generally with only a single opening per side (C00-04, C06-00), both 2D models perform comparatively well, and succeed in reproducing the number and relative size of flow recirculations.
- In a limited number of configurations (C1, C4 and C5), leading to particularly complex patterns of flow recirculations, neither Model 1 nor Model 2 correctly predict the flow patterns. In Configuration C19-12, the number of computed recirculations by both models is in line with the experimental observations; but their relative sizes diverge from the observations.
- In all other cases (with only one exception, C06-04), Model 2 provides a better prediction of the flow field than Model 1 does. In Configuration C00-12, the number of large recirculations computed by Model 2 is correct, while it is not for Model 1. In Configuration C19-00, the right upstream recirculation is computed by Model 2, while Model 1 fails to capture it. Similarly, in Configuration C2, the smaller recirculation in the top left corner is predicted by Model 2 while it is not by Model 1. In Configuration C3, the flow field computed by Model 2 is also closer to the experimental observations than the one predicted by Model 1.
- Only in Configuration C06-04, Model 1 provides a flow field more similar to the experimental one.

Therefore, although Model 1 performs better than Model 2 for the prediction of the outflow discharge partition, this does not hold true for predicting the flow field within the urban block.

Moreover, the constant eddy viscosity used in Model 1 (value of 1 $m^2/s$) was carefully set based on the modeler's past experience in reproducing reduced-scale laboratory experiments (Paquier et al., 2020; 2022). However, this value of a dimensional quantity has limited chance to be transferrable across scales, particularly for the application of the model to real-world examples. This is another advantage of Model 2 (with a depth-averaged $k$-$\varepsilon$ turbulence closure) over Model 1, as in Model 2 the parameters of the turbulence closure are all non-dimensional and, as such, they are not changed when applying the model at different scales (e.g., laboratory experiment vs. real-world application). This aspect was discussed earlier by Bruwier et al. (2017).

**Table 3.** Qualitative appraisal of the agreement between observed and computed flow patterns. Notation "L" stands for "large recirculation", "S" for "smaller recirculation(s)" and "s" for "even smaller recirculation(s)". Green, red and orange shaded cells indicate, respectively, a good, fair, and poor agreement between the computations and the observations.

| Configuration | Experimental | Model 1 | Model 2 |
|---|---|---|---|
| C00-00 | Only small recirculations in the branches downstream of junctions | | |
| C100-100 | 2L | 2L | 2L |
| C00-04 | 2L | 2L | 2L |
| C00-12 | 2L + 5S | 1L + 6S | 2L + 3S |
| C06-00 | 2L | 2L | 2L |
| C19-00 | 1L + 4S | 1L + 2S | 1L + 3S + 1s |
| C06-04 | 2L + 1S | 2L + 1S | 2L + 1S (though too big) |
| C19-12 | 2L + 3S | 2L (incorrect relative sizes) + 3S | 2L (incorrect relative sizes) + 3S |
| C1 | 3L | 3L (incorrect shape) | 4L (incorrect shape) |
| C2 | 2L + 1S | 2L | 2L + 1S |
| C3 | 2L + 2S + 3s | 2L + 4S (incorrect shapes) | 2L+ 2S |
| C4 | 2L + 2S + 2s | 1L + 4S (incorrect shapes) | 1L + 5S (incorrect shapes) |
| C5 | 1L + 4S | 2L + 1S (incorrect shapes) | 2L + 1S (incorrect shapes) |

## 3.3. Unsteady flow tests

### *3.3.1. Flow depths*

The unsteady flow simulations were carried out only with Model 1. The presence of hydraulic jumps at different locations in the experiments and in the calculations, causes a lower agreement of peak flow depths compared to the steady flow cases, with an average deviation of 6.7% between calculations and measurements in the streets around the block. Model 1 slightly overestimates the peak flow depth in the

Right Street, which is the highest peak flow depth in the test domain, with an error of less than 4% (Figure 8). The model performs best in the Right Street for $\phi$ = 0.75, for every tested hydrograph (H.LSS, H.LLL, and H.SLS). No trend is detected between the rest of the block porosities and the performance of the model in predicting peak flow depths in the Right Street. The absolute error in the other three streets around the block is similar to that in the Right Street; however, the peak flow depth is lower and thus, percentagewise Model 1 is less accurate in predicting flow depths there. In these three streets, Model 1 predicts flow depths best in H.SLS (the hydrograph with the greatest unsteadiness), followed by H.LLL and H.LSS. The predictive performance of the model in the H.SLS hydrograph deteriorates with decreasing block porosity, whereas for H.LLL and H.LSS there is a more erratic pattern on the agreement between depth modelling results and measurements. For all flow cases, the flow depth is underestimated in the Left Street (Figure 8) and in the block (Figure S5 in the Supplementary Material).

Figure 9 shows how the flow depth evolves in time at different measuring locations (Figure 1b) of the test domain for the hydrograph H.LSS and $\phi$ = 1, i.e., the block without any interior obstruction. The model captures the evolution of the flow depths in the Right, Left, and Upstream Street relatively accurately after the first 60 seconds, particularly in the rising limb of the hydrograph; however, it cannot correctly reproduce the flow depth at the location $P_{in}$.

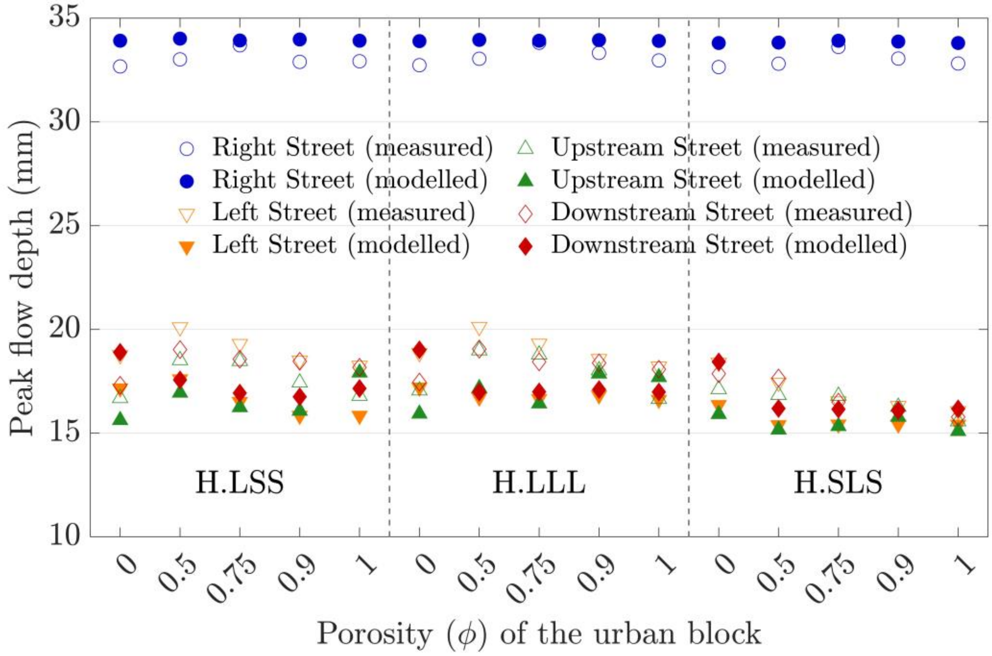


**Figure 8.** Measurements and calculations with Model 1 of peak flow depths in the streets around the porous block (locations $P_{RS}$, $P_{LS}$, $P_{US}$, and $P_{DS}$ in Figure 1b for the Right, Left, Upstream, and Downstream Street, respectively) for the three cases with unsteady hydrographs (H.LSS, H.LLL, and H.SLS). The tested urban blocks and their respective porosities are shown in Figure 2c. The vertical dashed lines separate the data for each flow case.

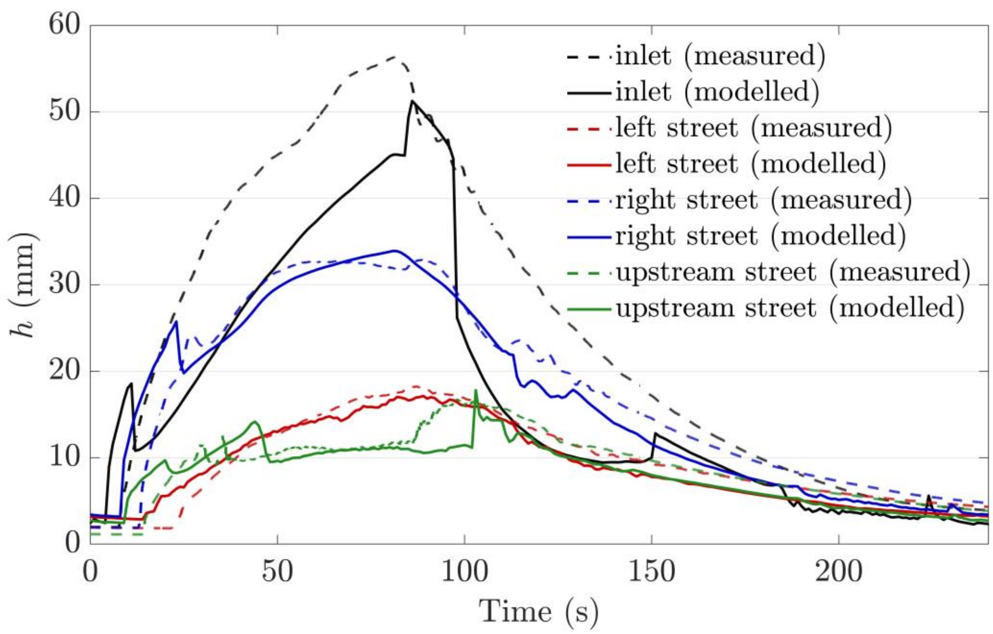


**Figure 9.** Measured and calculated (with Model 1) flow depths (locations $P_{in}$, $P_{RS}$, $P_{LS}$, and $P_{US}$ in Figure 1b for the inlet and the Right, Left, and Upstream Street, respectively) as a function of time for the H.LSS discharge hydrograph with porosity $\phi$ = 1 (series 3).

### 3.3.2. *Discharge partition*

For steady flow in the configurations of test series 3 (Figure 2c), the discharge at Outlet 4 is miscalculated by approximately 0.05 l/s on average, while the discharge at Outlet 2 is underestimated by about 0.1 l/s (Figure 10). As for test series 1 and 2 (Figure 2a, b), the downstream boundary conditions should be adapted to obtain a more correct distribution. However, it should be noted that changing critical flow to free outflow at Outlets 1 and 2 (in which the flow is partly supercritical) did not change the outflow distribution. The discharges at the outlets for the steady flow case of test series 3 exhibit a slightly increasing trend with increasing porosity in Outlet 2 and rather constant values, besides $\phi = 0$, in the other outlets (Figure 10).

For the unsteady flows, the peak outflow discharge in Outlet 1 is consistently higher than the peak discharges in the other outlets for every tested hydrograph and porosity value, as for the respective steady flow test (Figure 10). The outflow in Outlet 1 becomes the highest when the block has no porosity ($\phi$ = 0), while it reaches a plateau for each flow case when the block has porosity. For the unsteady cases, Model 1 predicts accurately the peak discharge in Outlet 1 for the non-porous block, for every hydrograph, but it overestimates this peak discharge by less than 4% for the porous blocks. Model 1 performs even better in predicting the peak discharge in Outlet 1 in the steady flow case, with a slight underestimation of the non-porous block case and a few overestimations for the porous block cases. The second highest peak outflow discharge occurs in Outlet 4, where Model 1 overestimates the peak discharge by around 0.085 l/s for the non-porous block, for all flow cases (Figure 10). The predictive performance of Model 1 mostly deteriorates with increasing porosity of the block for all three hydrographs, particularly for H.SLS, while this is not observed in the steady flow cases, where only a slight overestimation is noted. The overestimations in Outlets 1 and 4 are partially compensated by some underestimations in the peak outflow discharge in Outlet 2, where, percentagewise, the model predictions deviate from the measurements the most for all flow cases, besides the hydrograph H.SLS. Finally, Model 1 predicts accurately the peak outflow discharge in Outlet 3. Overall, for all unsteady cases the average discrepancy between calculations and measurements of the peak discharges at the outlets is 8.6%. A comparison between the measured and modelled peak flow depths at the locations $P_{out1}$ - $P_{out4}$ near the outlets (Figure 1b) is provided in Figure S6 in the Supplementary Material.

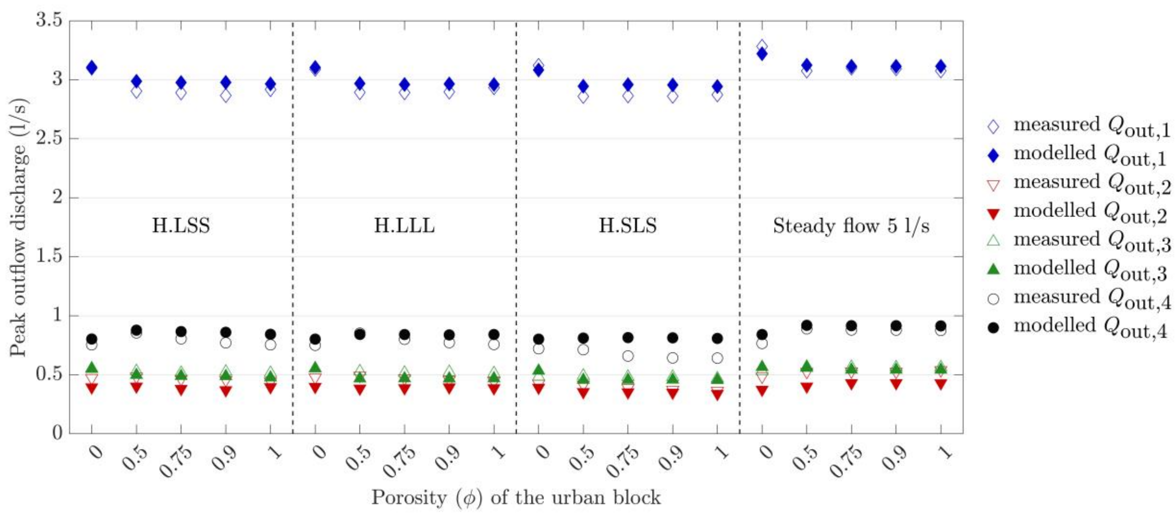


**Figure 10.** Measured and calculated (with Model 1) peak discharges at the four outlets of the experimental setup of Figure 1b for the three cases with unsteady hydrographs (H.LSS, H.LLL, and H.SLS) and a steady flow case with inflow discharge of 5 l/s, which is equal to the peak value of each unsteady hydrograph at the inlet. The tested urban blocks and their respective porosities are shown in Figure 2c. The vertical dashed lines separate the data for each flow case.

### *3.3.3. Velocity flow fields*

As in Section 3.2.3, the depth-averaged flow velocities modelled with 2D SWE are compared to the surface velocities measured with LSPIV. For $\phi$ = 1 in steady flow, the flow pattern of the third series is similar to C06-04 with two main nearly symmetrical recirculation zones (Figure 11). For the unsteady case with the hydrograph H.LSS (with the greatest unsteadiness), after the flow peak the flow pattern remains quite similar for a long time. The initial part of this process is reproduced well by Model 1. Before the flow peak, the block is filling and the observed flow pattern comprises four main recirculation zones that are not reproduced by Model 1, which, instead, generates a flow pattern that tends more rapidly to a flow pattern with two main recirculation zones. Reducing $\phi$ leads to reduced water volume in the block and an increase in the number of recirculation zones within the porous block, which are fairly well reproduced by Model 1 (Figure 12).

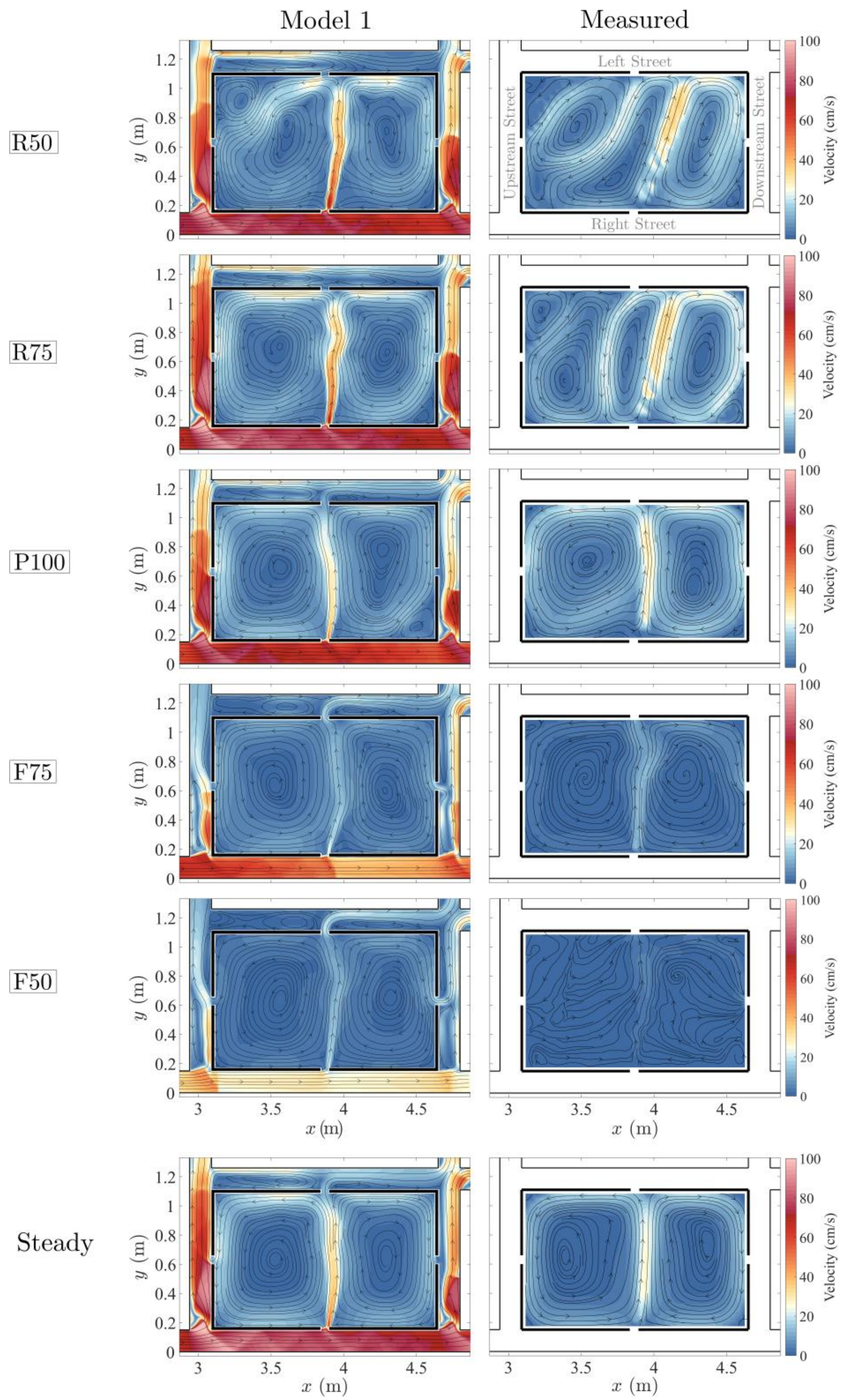


**Figure 11.** Quasi-instantaneous surface velocities modelled with Model 1 (left column) and measured (right column) for the hydrograph H.LSS and $\phi = 1$. All experimental configurations were obtained from Mejia-Morales et al. (2022a). In the first column, R, P, and F stand for rising, peak, and falling stage of the hydrograph, while the numbers 50, 75, and 100 show the ratio of the flow depth to the maximum flow depth within the porous block at that instant.

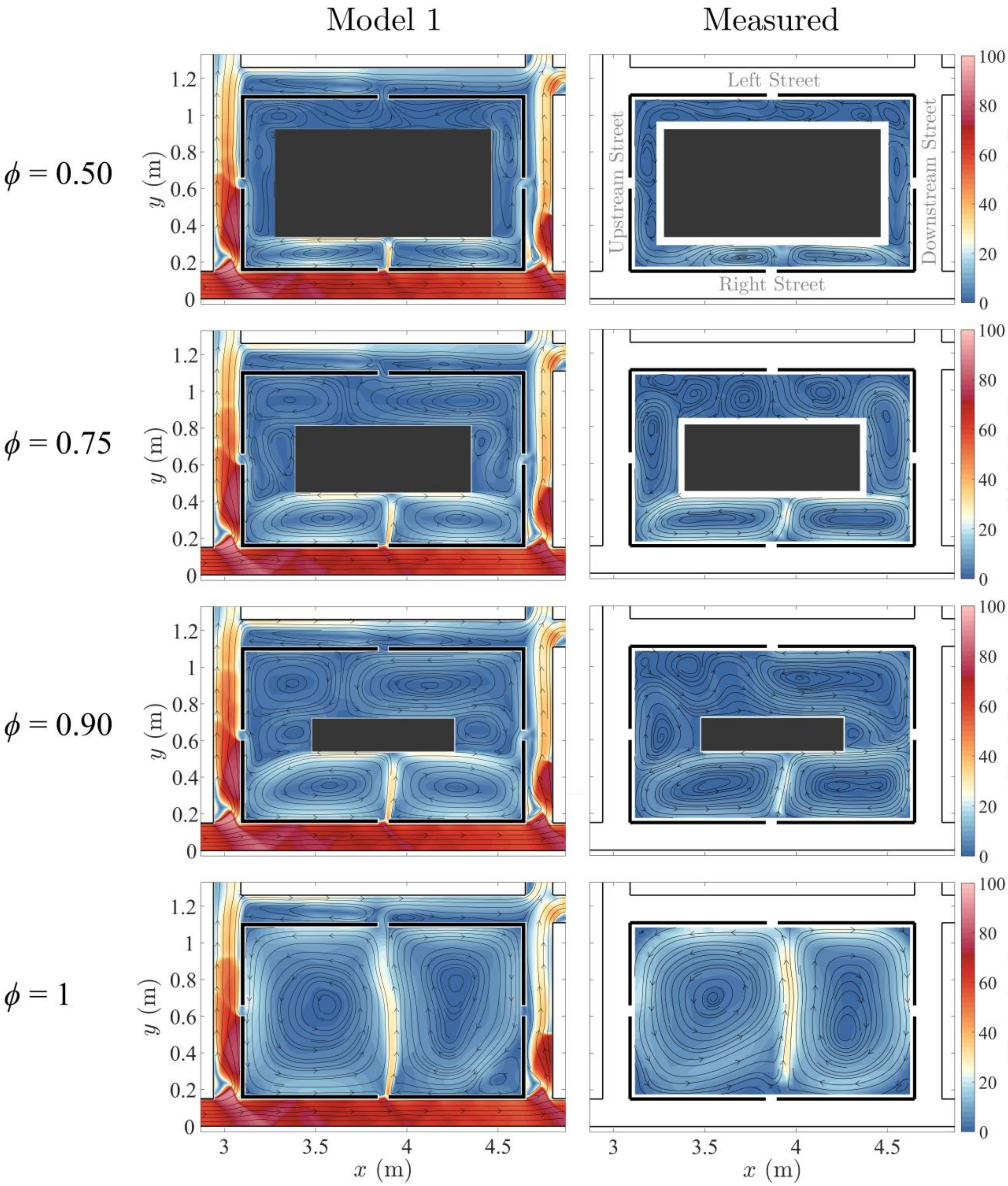


**Figure 12.** Quasi-instantaneous depth-averaged velocities modelled with Model 1 (left column) and surface velocities measured (right column) at the peak of the hydrograph H.LSS with various values of $\phi$. All experimental configurations were obtained from Mejia-Morales et al. (2022a).

## 4. Conclusions

Accurate and fast computational tools for the estimation of urban flood hazard are of vital importance. Although in such cases the flow can be 3D in parts of the urban layout, it is important from a management perspective to understand when these 3D processes are dominant and when the flow can be reliably modelled with 2D shallow water equations. In this paper, we demonstrated the capacity of two 2D shallow water flow solvers to simulate urban floods involving flow exchanges with the interior of an urban block in nineteen idealized urban layouts. The computations were compared against published and new experimental observations in steady and unsteady conditions. The tested computational models differed mostly by the turbulence closure used for estimating the eddy viscosity.

Both models reproduced accurately the measured flow depth for all cases. The prediction of the discharge distribution and the flow velocity patterns within and around the urban block was in general satisfactory but deteriorated when the flow exchanges between the urban block and the surrounding streets increased and became asymmetrical. The average difference between the modelled discharge distributions and the measurements at the outlets was 2.5% and 7.3% for Model 1 and Model 2, respectively. With respect to the flow velocities, none of the two models outperformed consistently the other, which implies that both tested turbulence closure models are suitable to model the flow patterns within and around an urban block, although with different accuracy at different flow patterns.

For unsteady conditions, the difficulties increased because of the occurrence of hydraulic jumps and the sequence of a filling phase and an emptying phase of the block. The error thus rose in parameters such as the peak flow depths in the streets and the peak discharges at the outlets, which were miscalculated by 6.7% and 8.6%, respectively. However, the influence of the porosity of the urban block was generally simulated in the right way and except during rapid filling of the block, the computed velocity pattern inside the block reproduced sufficiently well the main process.

Even if the discharge partition at the outlets is only a little sensitive to a change in the urban block openings, local modifications of the flow field can be particularly important for urban planning under climate change scenarios, since the building density and the distance between neighboring buildings are the most influential parameters affecting pluvial flooding (Bruwier et al., 2020).

The geometric configurations considered here are highly simplified compared to real-world urbanized floodplains, which have considerably more intricate flowpaths, street profiles, opening shapes and indoor arrangement of buildings. In addition, in reality the flow exchanges between the streets and the urban blocks are influenced by obstructions near the openings such as parked cars and street furniture (Mignot et al., 2020) and the interaction of surface flows with surcharging sewers (Kitsikoudis et al., 2021). These aspects highlight the limitations of the present study and need to be investigated in future studies with either large scale experiments or field data to additionally address potential scale effects that affected our results. In practice, evaluating accurately the flow intrusion into buildings and building blocks would require particularly fine mesh resolution in the near field of the opening, or the use of parametrizations such as weir equations. Such aspects affect the operationality of models for simulating large urban floodplains and need to be investigated. The performance of 1D modelling in the streets, combined with side discharge equations for the exchanges through building opening, could also be investigated in a follow-up study.

## Acknowledgements

The authors from INRAE and INSA Lyon acknowledge the financial support offered by the French National Research Agency (ANR) for the project DEUFI (under grant ANR-18-CE01-0020). The authors gratefully acknowledge MSc students Yann Nicol and Eliott Crestey who contributed to the numerical computations. Insightful comments by the Editor and three anonymous Reviewers have contributed to significantly improve the quality of the manuscript.

## Data availability

All experimental observations used in this research are available at: https://doi.org/10.57745/UJOCJ8 (Mejia-Morales et al., 2022b).

## Authors' contributions

The study was designed by A.P., B.D., S.P., and E.M., who also defined the methodology; all laboratory experiments were conducted by M.M.M., under the supervision of S.P. and E.M.; computations with Model 1 were conducted by A.P. and those with Model 2 by students under the guidance of P.A., B.D., S.E., and M.P. The original draft of the manuscript was prepared by V.K. with the support of B.D., A.P., and M.M.M. It was revised by V.K., B.D., E.M. and S.P.

## References


Addison-Atkinson, W., Chen, A. S., Memon, F. A., Chang, T.-J. (2022). Modelling urban sewer flooding and quantitative microbial risk assessment: A critical review. *Journal of Flood Risk Management* **15**(**4**), e12844. https://doi.org/10.1111/jfr3.12844

Almeida, G. A. M. de, Bates, P., Ozdemir, H. (2018). Modelling urban floods at submetre resolution: challenges or opportunities for flood risk management? *Journal of Flood Risk Management* **11**, S855–S865. https://doi.org/10.1111/jfr3.12276

Arrault, A., Finaud-Guyot, P., Archambeau, P., Bruwier, M., Erpicum, S., Pirotton, M., Dewals, B. (2016). Hydrodynamics of long-duration urban floods: experiments and numerical modelling. *Natural Hazards and Earth System Sciences* **16**(**6**), 1413–1429. https://doi.org/10.5194/nhess-16-1413-2016

Arrighi, C., Oumeraci, H., Castelli, F. (2017). Hydrodynamics of pedestrianstextquotesingle instability in floodwaters. *Hydrology and Earth System Sciences* **21**(**1**), 515–531. https://doi.org/10.5194/hess-21-515-2017

Bates, P. D. (2022). Flood Inundation Prediction. *Annual Review of Fluid Mechanics* **54**(**1**), 287–315. https://doi.org/10.1146/annurev-fluid-030121-113138

Bazin, P.-H., Mignot, E., Paquier, A. (2017). Computing flooding of crossroads with obstacles using a 2D numerical model. *Journal of Hydraulic Research* **55**(**1**), 72–84. https://doi.org/10.1080/00221686.2016.1217947

Bazin, P.-H., Nakagawa, H., Kawaike, K., Paquier, A., Mignot, E. (2014). Modeling Flow Exchanges between a Street and an Underground Drainage Pipe during Urban Floods. *Journal of Hydraulic Engineering* **140**(**10**), 04014051. https://doi.org/10.1061/(asce)hy.1943-7900.0000917

Bernardini, G., Quagliarini, E., D'Orazio, M., Brocchini, M. (2020). Towards the simulation of flood evacuation in urban scenarios: Experiments to estimate human motion speed in floodwaters. *Safety Science* **123**, 104563. https://doi.org/10.1016/j.ssci.2019.104563

Birkmann, J., Welle, T., Solecki, W., Lwasa, S., Garschagen, M. (2016). Boost resilience of small and mid-sized cities. *Nature* **537**(**7622**), 605–608. https://doi.org/10.1038/537605a

Brown, R., Chanson, H. (2013). Turbulence and Suspended Sediment Measurements in an Urban Environment during the Brisbane River Flood of January 2011. *Journal of Hydraulic Engineering* **139**(**2**), 244–253. https://doi.org/10.1061/(asce)hy.1943-7900.0000666

Bruwier, M., Erpicum, S., Archambeau, P., Pirotton, M., Dewals, B. (2017). Discussion of: Computing flooding of crossroads with obstacles using a 2D numerical model. *Journal of Hydraulic Research* **55**(**5**), 737–741. https://doi.org/10.1080/00221686.2017.1326406

Bruwier, M., Maravat, C., Mustafa, A., Teller, J., Pirotton, M., Erpicum, S., Archambeau, P., Dewals, B. (2020). Influence of urban forms on surface flow in urban pluvial flooding. *Journal of Hydrology* **582**, 124493. https://doi.org/10.1016/j.jhydrol.2019.124493

Camnasio, E., Erpicum, S., Archambeau, P., Pirotton, M., Dewals, B. (2014). Prediction of mean and turbulent kinetic energy in rectangular shallow reservoirs. *Engineering Applications of Computational Fluid Mechanics* **8**(**4**), 586–597. https://doi.org/10.1080/19942060.2014.11083309

Chang, T.-J., Wang, C.-H., Chen, A. S., Djordjevic, S. (2018). The effect of inclusion of inlets in dual drainage modelling. *Journal of Hydrology* **559**, 541–555. https://doi.org/10.1016/j.jhydrol.2018.01.066

Chen, D., Acharya, K., Stone, M. (2010). Sensitivity Analysis of Nonequilibrium Adaptation Parameters for Modeling Mining-Pit Migration. *Journal of Hydraulic Engineering* **136**(**10**), 806–811. https://doi.org/10.1061/(asce)hy.1943-7900.0000242

Chen, S., Huang, Q., Muttarak, R., Fang, J., Liu, T., He, C., Liu, Z., Zhu, L. (2022). Updating global urbanization projections under the Shared Socioeconomic Pathways. *Scientific Data* **9**(**137**). https://doi.org/10.1038/s41597-022-01209-5

Chen, W., Wang, X., Deng, S., Liu, C., Xie, H., Zhu, Y. (2019). Integrated urban flood vulnerability assessment using local spatial dependence-based probabilistic approach. *Journal of Hydrology* **575**, 454–469. https://doi.org/10.1016/j.jhydrol.2019.05.043

Chen, Y., Zhou, H., Zhang, H., Du, G., Zhou, J. (2015). Urban flood risk warning under rapid urbanization. *Environmental Research* **139**, 3–10. https://doi.org/10.1016/j.envres.2015.02.028

Costabile, P., Costanzo, C., Lorenzo, G. D., Macchione, F. (2020). Is local flood hazard assessment in urban areas significantly influenced by the physical complexity of the hydrodynamic inundation model? *Journal of Hydrology* **580**, 124231. https://doi.org/10.1016/j.jhydrol.2019.124231

Dewals, B., Bruwier, M., Pirotton, M., Erpicum, S., Archambeau, P. (2021). Porosity Models for Large-Scale Urban Flood Modelling: A Review. *Water* **13**(**7**), 960. https://doi.org/10.3390/w13070960

Dewals, B., Erpicum, S., Archambeau, P., Pirotton, M. (2012). Discussion of: Experimental study of velocity fields in rectangular shallow reservoirs. *Journal of Hydraulic Research* **50**(**4**), 435–436. https://doi.org/10.1080/00221686.2012.702856

Doocy, S., Daniels, A., Murray, S., Kirsch, T. D. (2013). The Human Impact of Floods: a Historical Review of Events 1980-2009 and Systematic Literature Review. *PLoS Currents*. https://doi.org/10.1371/currents.dis.f4deb457904936b07c09daa98ee8171a

Dottori, F., Figueiredo, R., Martina, M. L. V., Molinari, D., Scorzini, A. R. (2016). INSYDE: a synthetic, probabilistic flood damage model based on explicit cost analysis. *Natural Hazards and Earth System Sciences* **16**(**12**), 2577–2591. https://doi.org/10.5194/nhess-16-2577-2016

El Kadi Abderrezzak, K., Lewicki, L., Paquier, A., Rivière, N., Travin, G. (2011). Division of critical flow at three-branch open-channel intersection. *Journal of Hydraulic Research* **49**(**2**), 231–238. https://doi.org/10.1080/00221686.2011.558174

El Kadi Abderrezzak, K., Paquier, A. (2009). Discussion of "Numerical and Experimental Study of Dividing Open-Channel Flows" by A. S. Ramamurthy, Junying Qu, and Diep Vo. *Journal of Hydraulic Engineering* **135**(**12**), 1111–1112. https://doi.org/10.1061/(asce)hy.1943-7900.0000009

Erpicum, S., Dewals, B. J., Archambeau, P., Pirotton, M. (2010). Dam break flow computation based on an efficient flux vector splitting. *Journal of Computational and Applied Mathematics* **234**(**7**), 2143–2151. https://doi.org/10.1016/j.cam.2009.08.110

Erpicum, S., Meile, T., Dewals, B. J., Pirotton, M., Schleiss, A. J. (2009). 2D numerical flow modeling in a macro-rough channel. *International Journal for Numerical Methods in Fluids* **61**(**11**), 1227–1246. https://doi.org/10.1002/fld.2002

Fujita, I., Muste, M., Kruger, A. (1998). Large-scale particle image velocimetry for flow analysis in hydraulic engineering applications. *Journal of Hydraulic Research* **36**(**3**), 397–414. https://doi.org/10.1080/00221689809498626

Gems, B., Mazzorana, B., Hofer, T., Sturm, M., Gabl, R., Aufleger, M. (2016). 3-D hydrodynamic modelling of flood impacts on a building and indoor flooding processes. *Natural Hazards and Earth System Sciences* **16**(**6**), 1351–1368. https://doi.org/10.5194/nhess-16-1351-2016

Gross, M. (2016). The urbanisation of our species. *Current Biology* **26**(**23**), R1205–R1208. https://doi.org/10.1016/j.cub.2016.11.039

Guo, K., Guan, M., Yu, D. (2021). Urban surface water flood modelling – a comprehensive review of current models and future challenges. *Hydrology and Earth System Sciences* **25**(**5**), 2843–2860. https://doi.org/10.5194/hess-25-2843-2021

Haltas, I., Tayfur, G., Elci, S. (2016). Two-dimensional numerical modeling of flood wave propagation in an urban area due to Ürkmez dam-break, Izmir, Turkey. *Natural Hazards* **81**(**3**), 2103–2119. https://doi.org/10.1007/s11069-016-2175-6

Heller, V. (2011). Scale effects in physical hydraulic engineering models. *Journal of Hydraulic Research* **49**(**3**), 293–306. https://doi.org/10.1080/00221686.2011.578914

Hettiarachchi, S., Wasko, C., Sharma, A. (2018). Increase in flood risk resulting from climate change in a developed urban watershed – the role of storm temporal patterns. *Hydrology and Earth System Sciences* **22**(**3**), 2041–2056. https://doi.org/10.5194/hess-22-2041-2018

Huang, J., Weber, L. J., Lai, Y. G. (2002). Three-Dimensional Numerical Study of Flows in Open-Channel Junctions. *Journal of Hydraulic Engineering* **128**(**3**), 268–280. https://doi.org/10.1061/(asce)0733-9429(2002)128:3(268)

Huggel, C., Stone, D., Auffhammer, M., Hansen, G. (2013). Loss and damage attribution. *Nature Climate Change* **3**(**8**), 694–696. https://doi.org/10.1038/nclimate1961

Idel'cik, I. E. (1969). Mémento des pertes de charge. Eyrolles (translated to French by Meury M).

Jongman, B. (2018). Effective adaptation to rising flood risk. *Nature Communications* **9**, 1986. https://doi.org/10.1038/s41467-018-04396-1

Khan, A. A., Cadavid, R., Wang, S. S.-Y. (2000). Simulation of channel confluence and bifurcation using the CCHE2D model. *Proceedings of the Institution of Civil Engineers - Water and Maritime Engineering* **142**(**2**), 97–102. https://doi.org/10.1680/wame.2000.142.2.97

Kitsikoudis, V., Becker, B. P. J., Huismans, Y., Archambeau, P., Erpicum, S., Pirotton, M., Dewals, B. (2020). Discrepancies in Flood Modelling Approaches in Transboundary River Systems: Legacy of the Past or Well-grounded Choices? *Water Resources Management* **34**(**11**), 3465–3478. https://doi.org/10.1007/s11269-020-02621-5

Kitsikoudis, V., Erpicum, S., Rubinato, M., Shucksmith, J. D., Archambeau, P., Pirotton, M., Dewals, B. (2021). Exchange between drainage systems and surface flows during urban flooding: Quasi-steady and dynamic modelling in unsteady flow conditions. *Journal of Hydrology* **602**, 126628. https://doi.org/10.1016/j.jhydrol.2021.126628

Kreibich, H., Bergh, J. C. J. M. van den, Bouwer, L. M., Bubeck, P., Ciavola, P., Green, C., Hallegatte, S., Logar, I., Meyer, V., Schwarze, R., Thieken, A. H. (2014). Costing natural hazards. *Nature Climate Change* **4**(**5**), 303–306. https://doi.org/10.1038/nclimate2182

Kreibich, H., Piroth, K., Seifert, I., Maiwald, H., Kunert, U., Schwarz, J., Merz, B., Thieken, A. H. (2009). Is flow velocity a significant parameter in flood damage modelling? *Natural Hazards and Earth System Sciences* **9**(**5**), 1679–1692. https://doi.org/10.5194/nhess-9-1679-2009

Leandro, J., Schumann, A., Pfister, A. (2016). A step towards considering the spatial heterogeneity of urban key features in urban hydrology flood modelling. *Journal of Hydrology* **535**, 356–365. https://doi.org/10.1016/j.jhydrol.2016.01.060

Li, X., Erpicum, S., Mignot, E., Archambeau, P., Pirotton, M., Dewals, B. (2021a). Influence of urban forms on long-duration urban flooding: Laboratory experiments and computational analysis. *Journal of Hydrology* **603**, 127034. https://doi.org/10.1016/j.jhydrol.2021.127034

Li, X., Erpicum, S., Mignot, E., Archambeau, P., Rivière, N., Pirotton, M., Dewals, B. (2020). Numerical Insights Into the Effects of Model Geometric Distortion in Laboratory Experiments of Urban Flooding. *Water Resources Research* **56**(**7**), e2019WR026774. https://doi.org/10.1029/2019wr026774

Li, X., Kitsikoudis, V., Mignot, E., Archambeau, P., Pirotton, M., Dewals, B., Erpicum, S. (2021b). Experimental and Numerical Study of the Effect of Model Geometric Distortion on Laboratory Modeling of Urban Flooding. *Water Resources Research* **57**(**10**), e2021WR029666. https://doi.org/10.1029/2021wr029666

Lin, J., He, X., Lu, S., Liu, D., He, P. (2021). Investigating the influence of three-dimensional building configuration on urban pluvial flooding using random forest algorithm. *Environmental Research* **196**, 110438. https://doi.org/10.1016/j.envres.2020.110438

Liu, L., Sun, J., Lin, B., Lu, L. (2018). Building performance in dam-break flow – an experimental study. *Urban Water Journal* **15**(**3**), 251–258. https://doi.org/10.1080/1573062x.2018.1433862
Luo, H., Fytanidis, D. K., Schmidt, A. R., Garcıa, M. H. (2018). Comparative 1D and 3D numerical investigation of open-channel junction flows and energy losses. *Advances in Water Resources* **117**, 120–139. https://doi.org/10.1016/j.advwatres.2018.05.012
Luo, P., Luo, M., Li, F., Qi, X., Huo, A., Wang, Z., He, B., Takara, K., Nover, D., Wang, Y. (2022). Urban flood numerical simulation: Research, methods and future perspectives. *Environmental Modelling and Software* **156**, 105478. https://doi.org/10.1016/j.envsoft.2022.105478
Lv, H., Wu, Z., Meng, Y., Guan, X., Wang, H., Zhang, X., Ma, B. (2022). Optimal Domain Scale for Stochastic Urban Flood Damage Assessment Considering Triple Spatial Uncertainties. *Water Resources Research* **58**(**7**), e2021WR031552. https://doi.org/10.1029/2021wr031552
Martinez-Gomariz, E., Forero-Ortiz, E., Russo, B., Locatelli, L., Guerrero-Hidalga, M., Yubero, D., Castan, S. (2021). A novel expert opinion-based approach to compute estimations of flood damage to property in dense urban environments. Barcelona case study. *Journal of Hydrology* **598**, 126244. https://doi.org/10.1016/j.jhydrol.2021.126244
Martinez-Gomariz, E., Gómez, M., Russo, B., Djordjevic, S. (2018). Stability criteria for flooded vehicles: a state-of-the-art review. *Journal of Flood Risk Management* **11**, S817–S826. https://doi.org/10.1111/jfr3.12262
Mejia-Morales, M. A., Mignot, E., Paquier, A., Proust, S. (2022a). Laboratory investigation into the effect of the storage capacity of a city block on unsteady urban flood flows. *Water Resources Research* **(under review)**.
Mejia-Morales, M. A., Mignot, E., Paquier, A., Proust, S. (2022b). Data set of a laboratory experiment on the impact of the conveyance porosity of an urban block on the flood risk assessment. Recherche Data Gouv, UNF:6:Md2Yh9DNuCDyRl3U3kNGCw== [fileUNF]. https://doi.org/10.57745/UJOCJ8
Mejia-Morales, M. A., Mignot, E., Paquier, A., Sigaud, D., Proust, S. (2021). Impact of the porosity of an urban block on the flood risk assessment: A laboratory experiment. *Journal of Hydrology* **602**, 126715. https://doi.org/10.1016/j.jhydrol.2021.126715
Mejia-Morales, M. A., Proust, S., Mignot, E., Paquier, A. (2020). Experimental and Numerical Modelling of the Influence of Street-Block Flow Exchanges During Urban Floods, in: Advances Hydroinformatics. Springer Singapore, 495–505. https://doi.org/10.1007/978-981-15-5436-0_39
Mignot, E., Camusson, L., Riviere, N. (2020). Measuring the flow intrusion towards building areas during urban floods: Impact of the obstacles located in the streets and on the facade. *Journal of Hydrology* **583**, 124607. https://doi.org/10.1016/j.jhydrol.2020.124607
Mignot, E., Dewals, B. (2022). Hydraulic modelling of inland urban flooding: Recent advances. *Journal of Hydrology* **609**, 127763. https://doi.org/10.1016/j.jhydrol.2022.127763
Mignot, E., Li, X., Dewals, B. (2019). Experimental modelling of urban flooding: A review. *Journal of Hydrology* **568**, 334–342. https://doi.org/10.1016/j.jhydrol.2018.11.001
Mignot, E., Paquier, A., Haider, S. (2006). Modeling floods in a dense urban area using 2D shallow water equations. *Journal of Hydrology* **327**(**1-2**), 186–199. https://doi.org/10.1016/j.jhydrol.2005.11.026
Mignot, E., Paquier, A., Rivière, N. (2008). Experimental and numerical modeling of symmetrical four-branch supercritical cross junction flow. *Journal of Hydraulic Research* **46**(**6**), 723–738. https://doi.org/10.1080/00221686.2008.9521918
Mignot, E., Zeng, C., Dominguez, G., Li, C.-W., Rivière, N., Bazin, P.-H. (2013). Impact of topographic obstacles on the discharge distribution in open-channel bifurcations. *Journal of Hydrology* **494**, 10–19. https://doi.org/10.1016/j.jhydrol.2013.04.023
Neal, J. C., Bates, P. D., Fewtrell, T. J., Hunter, N. M., Wilson, M. D., Horritt, M. S. (2009). Distributed whole city water level measurements from the Carlisle 2005 urban flood event and comparison with hydraulic model simulations. *Journal of Hydrology* **368**(**1-4**), 42–55. https://doi.org/10.1016/j.jhydrol.2009.01.026

Neary, V. S., Sotiropoulos, F., Odgaard, A. J. (1999). Three-Dimensional Numerical Model of Lateral-Intake Inflows. *Journal of Hydraulic Engineering* **125**(**2**), 126–140. https://doi.org/10.1061/(asce)0733-9429(1999)125:2(126)

Ozdemir, H., Sampson, C. C., Almeida, G. A. M. de, Bates, P. D. (2013). Evaluating scale and roughness effects in urban flood modelling using terrestrial LIDAR data. *Hydrology and Earth System Sciences* **17**(**10**), 4015–4030. https://doi.org/10.5194/hess-17-4015-2013

Paquier, A., Mangara, C., Mignot, E., Li, X., & Dewals, B. (2022). 2-D Simulation of Flow Entering a Building. In Advances in Hydroinformatics: Models for Complex and Global Water Issues—Practices and Expectations (pp. 291-302). Singapore: Springer Nature Singapore.

Perks, M. T., Russell, A. J., Large, A. R. G. (2016). Technical Note: Advances in flash flood monitoring using unmanned aerial vehicles (UAVs). *Hydrology and Earth System Sciences* **20**(**10**), 4005–4015. https://doi.org/10.5194/hess-20-4005-2016

Pfahl, S., O'Gorman, P. A., Fischer, E. M. (2017). Understanding the regional pattern of projected future changes in extreme precipitation. *Nature Climate Change* **7**(**6**), 423–427. https://doi.org/10.1038/nclimate3287

Postacchini, M., Bernardini, G., D'Orazio, M., Quagliarini, E. (2021). Human stability during floods: Experimental tests on a physical model simulating human body. *Safety Science* **137**, 105153. https://doi.org/10.1016/j.ssci.2020.105153

Qi, W., Ma, C., Xu, H., Zhao, K., Chen, Z. (2022). A comprehensive analysis method of spatial prioritization for urban flood management based on source tracking. *Ecological Indicators* **135**, 108565. https://doi.org/10.1016/j.ecolind.2022.108565

Ramamurthy, A. S., Qu, J., Vo, D. (2007). Numerical and Experimental Study of Dividing Open-Channel Flows. *Journal of Hydraulic Engineering* **133**(**10**), 1135–1144. https://doi.org/10.1061/(asce)0733-9429(2007)133:10(1135)

Re, M., Kazimierski, L. D., Garcia, P. E., Ortiz, N. E., Lagos, M. (2022). Assessment of crowdsourced social media data and numerical modelling as complementary tools for urban flood mitigation. *Hydrological Sciences Journal* **67**(**9**), 1295–1308. https://doi.org/10.1080/02626667.2022.2075266

Rodi, W. (2017). Turbulence Modeling and Simulation in Hydraulics: A Historical Review. *Journal of Hydraulic Engineering* **143**(**5**), 03117001. https://doi.org/10.1061/(asce)hy.1943-7900.0001288

Roger, S., Dewals, B. J., Erpicum, S., Schwanenberg, D., Schüttrumpf, H., Köngeter, J., Pirotton, M. (2009). Experimental and numerical investigations of dike-break induced flows. *Journal of Hydraulic Research* **47**(**3**), 349–359. https://doi.org/10.1080/00221686.2009.9522006

Rosenzweig, B. R., Cantis, P. H., Kim, Y., Cohn, A., Grove, K., Brock, J., Yesuf, J., Mistry, P., Welty, C., McPhearson, T., Sauer, J., Chang, H. (2021). The Value of Urban Flood Modeling. *Earth's Future* **9**(**1**), e2020EF001739. https://doi.org/10.1029/2020ef001739

Rubinato, M., Helms, L., Vanderlinden, M., Hart, J., Martins, R. (2022). Flow exchange, energy losses and pollutant transport in a surcharging manhole linked to street profiles. *Journal of Hydrology* **604**, 127201. https://doi.org/10.1016/j.jhydrol.2021.127201

Sanderson, B. M., Wobus, C., Mills, D., Zarakas, C., Crimmins, A., Sarofim, M. C., Weaver, C. (2019). Informing Future Risks of Record-Level Rainfall in the United States. *Geophysical Research Letters* **46**(**7**), 3963–3972. https://doi.org/10.1029/2019gl082362

Schindfessel, L., Creëlle, S., Mulder, T. D. (2015). Flow Patterns in an Open Channel Confluence with Increasingly Dominant Tributary Inflow. *Water* **7**(**9**), 4724–4751. https://doi.org/10.3390/w7094724

Shettar, A. S., Murthy, K. K. (1996). A numerical study of division of flow in open channels. *Journal of Hydraulic Research* **34**(**5**), 651–675. https://doi.org/10.1080/00221689609498464

Smith, G. P., Modra, B. D., Felder, S. (2019). Full-scale testing of stability curves for vehicles in flood waters. *Journal of Flood Risk Management* **12**(**S2**). https://doi.org/10.1111/jfr3.12527

Sturm, M., Gems, B., Keller, F., Mazzorana, B., Fuchs, S., Papathoma-Köhle, M., Aufleger, M. (2018). Experimental analyses of impact forces on buildings exposed to fluvial hazards. *Journal of Hydrology* **565**, 1–13. https://doi.org/10.1016/j.jhydrol.2018.07.070

Van Emelen, S., Soares-Frazão, S., Riahi-Nezhad, C. K., Chaudhry, M. H., Imran, J., Zech, Y. (2012). Simulations of the New Orleans 17th Street Canal breach flood. *Journal of Hydraulic Research* **50**(**1**), 70–81. https://doi.org/10.1080/00221686.2011.642578

Wu, W. (2008). Computational River Dynamics. Taylor and Francis.

Wüthrich, D., Pfister, M., Schleiss, A. J. (2020). Forces on buildings with openings and orientation in a steady post-tsunami free-surface flow. *Coastal Engineering* **161**, 103753. https://doi.org/10.1016/j.coastaleng.2020.103753

Xia, J., Falconer, R. A., Wang, Y., Xiao, X. (2014). New criterion for the stability of a human body in floodwaters. *Journal of Hydraulic Research* **52**(**1**), 93–104. https://doi.org/10.1080/00221686.2013.875073

Xia, J., Teo, F. Y., Lin, B., Falconer, R. A. (2011). Formula of incipient velocity for flooded vehicles. *Natural Hazards* **58**(**1**), 1–14. https://doi.org/10.1007/s11069-010-9639-x

Yalcin, E. (2020). Assessing the impact of topography and land cover data resolutions on two-dimensional HEC-RAS hydrodynamic model simulations for urban flood hazard analysis. *Natural Hazards* **101**(**3**), 995–1017. https://doi.org/10.1007/s11069-020-03906-z

Yen, B. C. (2002). Open Channel Flow Resistance. *Journal of Hydraulic Engineering* **128**(**1**), 20–39. https://doi.org/10.1061/(asce)0733-9429(2002)128:1(20)

Zhou, Q., Leng, G., Huang, M. (2018). Impacts of future climate change on urban flood volumes in Hohhot in northern China: benefits of climate change mitigation and adaptations. *Hydrology and Earth System Sciences* **22**(**1**), 305–316. https://doi.org/10.5194/hess-22-305-2018

Zhou, Q., Yu, W., Chen, A. S., Jiang, C., Fu, G. (2016). Experimental Assessment of Building Blockage Effects in a Simplified Urban District. *Procedia Engineering* **154**, 844–852. https://doi.org/10.1016/j.proeng.2016.07.448